Tilt Pad Bearing Distributed Pad Inlet Temperature With Machine Learning—Part I: Static and Dynamic Characteristics

Jongin Yang[1]
Mem. ASME
Department of Mechanical Engineering,
Texas A&M University,
College Station, TX 77840
e-mail: jiyang@tamu.edu

Alan Palazzolo
Fellow ASME
Department of Mechanical Engineering,
Texas A&M University,
College Station, TX 77840
e-mail: a-palazzolo@tamu.edu

Uncertainty in mixing coefficients (MCs) for estimating pad leading-edge film temperature in tilt pad journal bearings reduces the reliability of predicted characteristics. A three-dimensional hybrid between pad (HBP) model, utilizing computational fluid dynamics (CFD) and machine learning (ML), is developed to provide the radial and axial temperature distributions at the leading edge. This provides an ML derived, two-dimensional film temperature distribution in place of a single uniform temperature. This has a significant influence on predicted journal temperature, dynamic coefficients, and Morton effect response. An innovative finite volume method (FVM) solver significantly increases computational speed, while maintaining comparable accuracy with CFD. Part I provides methodology and simulation results for static and dynamic characteristics, while Part II applies this to Morton effect response. [DOI: 10.1115/1.4052171]

Keywords: journal bearings, thermoelastohydrodynamic lubrication

1 Introduction

Cutting-edge turbomachinery demands extremely high, hydrodynamic bearing performance. Accurate static and dynamic characteristic prediction is imperative to ensure reliable machinery operation. This article proposes a new approach for improving the modeling accuracy for the most common hydrodynamic bearing, the tilting pad journal bearing (TPJB). This hybrid approach couples both computational fluid dynamics (CFD) and Reynolds models through the use of mixing coefficients (MCs) to provide economic and accurate solutions.

The Reynolds equation-based approach is commonly employed for bearing modeling due to its simplicity, fast computation, and noticeable progress with the thermo-elasto-hydrodynamic (TEHD) technique [1–10]. In 1964, Lund [1] first introduced the frequency-reduced dynamic coefficient concept. The dynamic coefficients are generally utilized in the rotordynamic analysis for predicting the stability, critical speed, and force response. In 1973, Tieu [2] employed the finite element method (FEM) to solve the Reynolds and energy equations in the fluid film to show the significances of the thermal effect. In 1987, Knight and Barrett [3] utilized a simplified one-dimensional Reynolds equation with an energy equation. In 1989, Brugier and Pascal [4] applied the generalized Reynolds equation to consider the three-dimensional (3D) temperature distribution in the fluid film. Pivot and pad flexibilities were involved with pad and journal thermal expansions. In 1990, Taniguchi et al. [5] investigated a turbulence effect, and the model took into account 3D thermal effects. In 1994, Kim et al. [6] studied the impact of pivot flexibility, pad flexibility, and thermal distortions of the shaft and pads. The researchers considered the generalized Reynolds and two-dimensional (2D) energy models for the fluid film. In 2015, Suh and Palazzolo [7] proposed a 3D approach for a TPJB. The generalized Reynolds and 3D energy equations were solved. The thermal and elastic deformations on pivot, pads, and shaft were also considered.

The groundbreaking research in Refs. [11–14] demonstrated that hydrodynamic bearing performance may be significantly affected by the oil feed conditions, which emphasizes the importance of accurate thermal mixing modeling between pads (BPs). Most conventional approaches apply Mixing theory to prescribe the leading-edge pad temperature in the fluid film. In 1967, Ettles [15] introduced the MC (or hot-carry-over-factor) to account for the degree of the heat flow mixing in a thrust bearing. The MC was substituted into the heat balance equation for leading-edge temperature in the fluid film. In 1983, Mitsui et al. [16] modified the MC for the consideration of the effect on preceding and next pad flows. The MC is equivalent to that presented in Pinkus's study [17]. In 2015, Suh and Palazzolo [7] corrected the MC in Mitsui's study to avoid the overestimated MC problem ($MC > 1$) when the preceding pad flow is higher than the next pad flow. There were recent studies to improve the conventional Mixing theory. In 2018, Haganmann and Schwarze [18] presented a BP model with a circular arc between pads considering a thermal effect. Instead of the MC, the approximated parameters, including effective supply temperature, mean upper BP temperature, and eddy conductivity, were defined for effective thermal boundary conditions. In 2019, Abdollahi and San Andres [19] introduced the mixing efficiency parameter, which was similar to the MC. The mixing efficiency parameter depends on the representative two flow conditions according to the existence of the recirculation flow or side leakage flow. The mixing was analyzed through a zero-dimensional heat balance for the BP.

Test results indicate that improvements in accuracy are still desired, even with the recent progress of the Reynolds model [18–23]. Reynolds approach mixing theories include uncertain or empirically derived parameters, such as the MC, mixing efficiency parameter, and effective thermal parameter, and the 3D mixing BP temperature distribution has been assumed or neglected. CFD solution of the full Navier–Stokes equations for the full bearing fluid domain could remove the inaccuracies in mixing theories. Recent studies have replaced the conventional Reynolds approach [1–7,15–19], with the CFD approach [20–25]. In 2017, Armentrout et al. [24] presented a single pad CFD model with turbulence effects. In 2019, Hagemann et al. [25] also employed a single pad CFD model, utilizing the film thickness of the Reynolds model solutions as an initial condition. In 2019, Yang and Palazzolo

[1]Corresponding author.

Contributed by the Tribology Division of ASME for publication in the JOURNAL OF TRIBOLOGY. Manuscript received November 26, 2020; final manuscript received August 11, 2021; published online September 3, 2021. Assoc. Editor: Patrick S. Keogh.

[20,21] developed a complete TEHD-CFD model for the TPJB static and dynamic coefficient analysis. The TEHD-CFD model was validated with test results in the author's extension work [22]. The CFD and TEHD-CFD results showed better accuracy than the TEHD-MC Reynolds model, indicating the importance of using an accurate (CFD predicted) leading-edge temperature prescription with the Reynolds model. The disadvantage of the full bearing CFD model approach is the massive computational resources and execution time required, rendering this impractical for obtaining dynamic coefficients in an industrial design setting. Consequently, a CFD supplemented Reynolds approach can provide a good balance between improved accuracy and reasonable computational load.

Yang and Palazzolo [23] proposed obtaining MC values from a machine learning (ML) approach utilizing CFD-calculated MC values for the respective training set. The machine learning-based mixing coefficient (MLMC) approach serves to remove the uncertainty of the presently assumed MC. The ML acts as a regression of the MC obtained from massive CFD-based data. This approach assumed a uniform temperature at a pad leading edge so that only a single MC was needed per pad. This is consistent with conventional Reynolds model practice; however, detailed CFD results show widely varying temperatures in the pad leading-edge film, especially with jet or nozzle oil supply between pads. This modeling deficiency is addressed in the present work, which develops an efficient and accurate means of providing and incorporating axial distributions of MC into the Reynolds model. Likewise, the leading-edge radial temperature distribution is included by utilizing a hybrid between pad (HBP) model with coupled 3D inner between pad (IBP) and one-dimensional (1D) outer between pad (OBP) models. Economical implementation of the approach is achieved by solving the energy equation utilizing a machine learning derived axial mixing coefficient (MLAMC) distribution, along with using the HBP model for improved accuracy. The finite volume method (FVM) is applied and is shown to significantly decrease computation time, and eliminate artificial temperature discontinuities, both improvements over the conventional FEM-based Reynolds and energy solvers [2–4,6,7]. The solution algorithms do not rely on commercial CFD software and are programed with commonly available programing codes (MATLAB, C/C++). The proposed model in this study is validated from the verified CFD work, and it is applied to the Morton effect (ME) simulation in Part II of this study.

Summarizing, the original contributions of Part I relative to the literature including the author's prior work include:

(a) A 3D, hybrid: finite volume—bulk thermal flow, between pad (HBP) model that trains a data-based ML regression of MCs, drag torque, and oil flowrate.
(b) Applying ML to a mixing coefficient MC axial distribution, accounting for the effects of discrete supply flow sources (nozzles), as opposed to a single MC at each pad leading edge.
(c) Prediction of a complete 2D temperature distribution at the pad leading edge, including radially and axially varying temperatures, which result from localized supply sources and significantly affects asymmetric journal heating in the Morton effect.
(d) Including a radial temperature distribution eliminates the need for a shaft temperature correction factor to calibrate the accuracy, which was introduced in the author's previous study.
(e) A novel FVM computation algorithm, embedded in a hybrid between pad solution, coupled with a FVM solution of the film equations shows equivalent accuracy as CFD, but with a much faster computational speed.
(f) Part I applies the novel modeling methodology for obtaining static equilibrium parameters and dynamic coefficients of a tilting pad journal bearing.

2 General Modeling Methodology

2.1 Overview—System and Component Models. Figure 1 shows the multiple solid and fluid computational domains needed to model the complex multiphysics interactions that occur in a TPJB. The TPJB in this study consists of five pad and one rotor (shaft) subdomains, with each pad domain described with its own fluid film, HBP, and pad solid domain. The HBP domains include the novel IBP and OBP subdomains, which provide 3D mass and energy continuities between pads. The boundary between IBP and OBP subdomains is defined by linear interpolation between the trailing-edge film of the prior pad and the leading-edge film thickness of the next pad. Table 1 summarizes the material types, theories, dimensions, numerical methods, and dependent variables for each domain. The FVM is adopted for assuring local mass and energy conservation in fluid-type domains. The FEM is used for its structural modeling versatility for solid-type domains.

The solution of the multiphysics, highly coupled system problem requires a consistency of variables over the adjoining boundaries of the subdomains, as explained as follows. The transient trajectories of the system converging to an equilibrium state are predicted through time integration (adaptive Runge–Kutta) of the dynamic rotor and flexible pad models coupled with the Reynolds model. The Reynolds model provides pressures (P), which integrate to forces applied to the journals in the rotordynamic models. The dynamic model's journal and pad displacements (x_R, y_R, x_p, y_p, and z_p) change the film thickness in the Reynolds model.

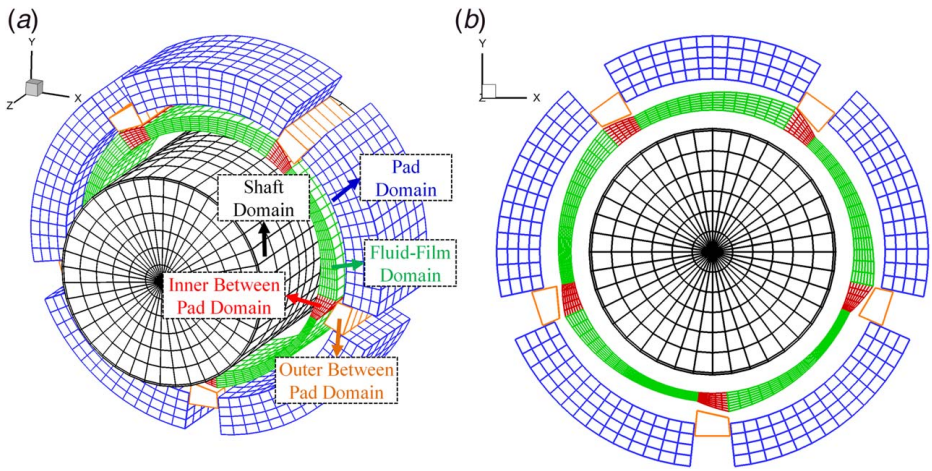

Fig. 1 Illustrations of computational domains for prediction of TPJB dynamic coefficients (magnified scale): (*a*) overall and (*b*) *x–y* view

Table 1 Summary of computational domains for dynamic coefficient prediction

Computational domain	Type	Theory	Dim.	Numerical integration		Dependent variable
				Space	Time	
Fluid film	Fluid	Reynolds	2D	FVM	–	P
		Energy	3D	FVM	–	T_f
Inner between pad	Fluid	Mass	3D	FVM	–	u_{IB}, v_{IB}, w_{IB}
		Energy	3D	FVM	–	T_{IB}
Outer between pad	Fluid	Mass	1D	FVM	–	w_{OB}
		Energy	1D	FVM	–	T_{OB}
Pad	Solid	TD	3D	FEM	–	x_{tp}, y_{tp}, z_{tp}
		DFP	3D	FEM	ARK	x_p, y_p, z_p
		Energy	3D	FEM	–	T_p
Rotor (shaft)	Solid	TD	3D	FEM	–	x_{tr}, y_{tr}, z_{tr}
		Energy	3D	FEM	–	T_R
Dynamic rotor	Solid	Rigid rotor	0D	–	ARK	x_R, y_R

Note: ARK: adaptive Runge–Kutta; DFP: dynamic flexible pad; Dim.: dimension; and TD: thermal deformation.

The Reynolds model provides the film velocity distributions required in the 3D energy equation, which provides temperatures to update the local lubricant dynamic viscosity, as an exponential function of fluid film temperature (T_f). The updated viscosity is imported into the Reynolds equation solution. The fluid film domain's 3D velocity field described earlier is determined from the pressure solution [7], and the velocities in the HBP (u_{IB}, v_{IB}, w_{IB}, and w_{OB}) are derived by the method described in Sec. 2.2.2. The energy equation is solved in both the fluid film and the HBP domains. The temperature solutions (T_{IB} and T_{OB}) in the HBP domains are utilized to determine the temperature at the pad leading-edge fluid film. The heat conduction problem in the solid domains is solved to obtain the temperature fields (T_p and T_R) after the equilibrium state is reached. The thermal deformations are then determined from the pad and rotor displacement solutions (x_{tp}, y_{tp}, z_{tp}, x_{tr}, y_{tr}, and z_{tr}). The film thickness is then updated in the Reynolds model using the thermal deformations. The aforementioned steps are iteratively repeated until the temperatures converge in all domains.

2.2 Fluid Film Model—Finite Volume Method

2.2.1 Generalized Reynolds and Three-Dimensional Energy Equation (Fluid Film). The generalized Reynolds equation [6] is utilized to include the 3D viscosity distribution in the fluid film and is given by

$$\nabla \cdot (D_1 \nabla P) + (\nabla D_2) \cdot U_s + \frac{\partial h_f}{\partial t} = 0 \tag{1}$$

$$D_1 = \int_0^{h_f} \int_0^z \frac{\xi}{\mu_f} d\xi dz - \int_0^{h_f} \frac{\xi}{\mu_f} d\xi \int_0^{h_f} \int_0^z \frac{1}{\mu_f} d\xi dz \Big/ \int_0^{h_f} \frac{1}{\mu_f} d\xi \tag{2}$$

$$D_2 = \int_0^{h_f} \int_0^z \frac{1}{\mu_f} d\xi dz \Big/ \int_0^{h_f} \frac{1}{\mu_f} d\xi \tag{3}$$

where P is the fluid film pressure, U_s is the rotating shaft surface velocity, and μ_f is the dynamic viscosity of the lubricant. The Reynolds equation (1) is derived by combining the continuity and momentum equations with the assumptions of incompressible Newtonian laminar flow, neglect of shaft curvature, and inertia effects. Film thickness expressions [7] for rigid and flexible pads are given by Eqs. (4) and (5), respectively:

$$\begin{aligned} h_f = {} & C_l, p - \{x_R + z\theta_y - x_{pvt}\cos(\theta_p)\}\cos(\theta) \\ & - \{y_R - z\theta_x - x_{pvt}\sin(\theta_p)\}\sin(\theta) \\ & - (C_{l,p} - C_{l,b})\cos(\theta - \theta_p) - \delta_{tlt} R_s \sin(\theta - \theta_p) - h_{R,TE} - h_{p,TE} \end{aligned} \tag{4}$$

$$h_{f,n} = \sqrt{(x_n - x_R - z_n\theta_y)^2 + (y_n - y_R + z_n\theta_x)^2} - R_s - h_{R,TE,n} - h_{p,TE,n} \tag{5}$$

where R_s is the shaft radius and θ_p is the pad's angular position. $C_{l,p}$ and $C_{l,b}$ are the radial pad and bearing clearances, respectively, n denotes the pad's node index, and x_R and y_R are the shaft center position coordinates. Figure 2 shows the journal and pad motion coordinates for the film thickness calculations. This study includes only cylindrical type pivots, with pivot deformation (x_{pvt}) and tilting motion (δ_{tlt}) coordinates for each pad. The film thickness equations also include the rotor's pitch (θ_x) and yaw (θ_y) angular displacements, and shaft and pad thermal deformations ($h_{R,TE}$, $h_{p,TE}$).

Dynamic viscosity (μ_f) is an important term in the Reynolds equation (1) for calculating pressures and is highly dependent on temperature via the equation $\mu_f = \mu_o e^{\alpha(T-T_o)}$ where μ_o is the reference dynamic viscosity, T_o is a reference temperature, and α is a viscosity coefficient. Suh and Palazzolo [26] demonstrated that the 3D energy equation may provide a significant increase in accuracy over the 2D model. Therefore, the present model uses the 3D energy equation:

$$\rho_f C_{p,f}\left(\frac{\partial T_f}{\partial t} + \mathbf{U} \cdot \nabla T_f\right) = \nabla \cdot (k_f \nabla T_f) + \mu_f \left[\left(\frac{\partial u}{\partial y}\right)^2 + \left(\frac{\partial w}{\partial y}\right)^2\right] \tag{6}$$

where ρ_f is the fluid density, $C_{p,f}$ is the fluid specific heat, k_f is the fluid thermal conductivity, and $\mathbf{U}$ is the velocity vector with components u, v, and w.

The Reynolds and energy equations are coupled via the dynamic viscosity and fluid velocity fields. Both equations are discretized forming systems of linear algebraic equations based on the FVM and solved. The discretization results from integrating the governing equations for a control volume (CV). The power law scheme is applied for the discretization of the convective and diffusive terms in the energy equation. The discretized equations for the control volume can be assembled into a global matrix form that

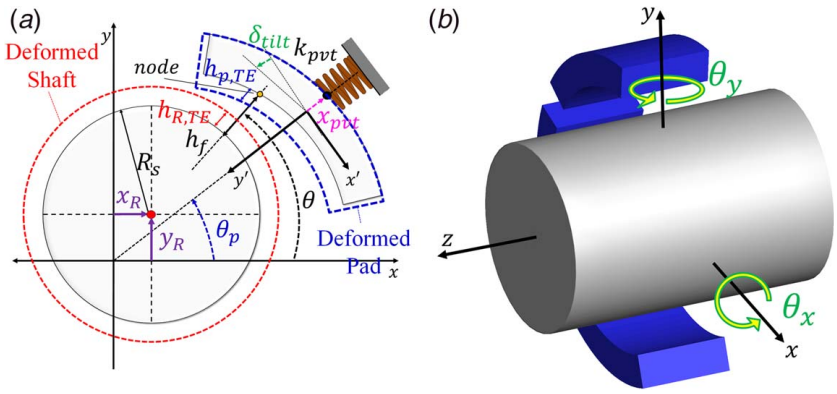

Fig. 2 Journal and pad motion coordinates for film thickness calculation: (*a*) *x–y* plane and (*b*) journal motion

includes the dependent variables of all control volumes, as shown in Eqs. (7) and (8):

Generalized Reynolds equation (global matrix form):

$$\underset{(N_f\times N_f)}{[K_f]}\ \underset{(N_f\times 1)}{\{P\}} = \underset{(N_f\times 1)}{\{F_f\}} \tag{7}$$

3D energy equation for fluid film (global matrix form):

$$\underset{(N_{T,f}\times N_{T,f})}{[C_{T,f}]}\ \underset{(N_{T,f}\times 1)}{\{\dot{T}_f\}} + \underset{(N_{T,f}\times N_{T,f})}{[K_{T,f}]}\ \underset{(N_{T,f}\times 1)}{\{T_f\}} = \underset{(N_{T,f}\times 1)}{\{F_{T,f}\}} \tag{8}$$

where the stiffness matrix and force vector of the Reynolds equation are $[K_f]$ and $\{F_f\}$, respectively, and $[C_{T,f}]$, $[K_{T,f}]$, and $\{F_{T,f}\}$ are the damping matrix, stiffness matrix, and force vector of the energy equation, respectively. The integers N_f and $N_{T,f}$ indicate the number of elements (CVs) for the Reynolds and energy equations, respectively.

The most computationally intensive part of the solution procedure is the rotor and pad dynamics solvers, coupled explicitly with the Reynolds model and implicitly with the energy equation, through the viscosities and film velocities. This results mainly from the use of a computationally intensive direct solution method and the simultaneous time integration of the governing structural dynamics equations. In addition, a fine mesh is required in the pad axial direction to accurately predict the fluid's axial temperature distribution [23]. Numerical tests showed that an alternative iterative solution method did not yield an improvement in computation speed because of convergence issue in the time integration solver. An efficient direct solution was ultimately developed for solving the Reynolds equation with the FVM. The core strategy is to minimize computational operations in the Gauss elimination by excluding operations involving zeros in the stiffness matrix (K_f) in Eq. (7). To illustrate the procedure consider solving Reynolds equation for 3×3 CVs, the discretized Reynolds equation can be written as follows:

$$\begin{pmatrix} a_{p,1} & -a_{t,1} & 0 & -a_{e,1} & 0 & 0 & 0 & 0 & 0 \\ -a_{b,2} & a_{p,2} & -a_{t,2} & 0 & -a_{e,2} & 0 & 0 & 0 & 0 \\ 0 & -a_{b,3} & a_{p,3} & -a_{t,3} & 0 & -a_{e,3} & 0 & 0 & 0 \\ -a_{w,1} & 0 & 0 & a_{p,4} & -a_{t,4} & 0 & -a_{e,4} & 0 & 0 \\ 0 & -a_{w,2} & 0 & -a_{b,5} & a_{p,5} & -a_{t,5} & 0 & -a_{e,5} & 0 \\ 0 & 0 & -a_{w,3} & 0 & -a_{b,6} & a_{p,6} & 0 & 0 & -a_{e,6} \\ 0 & 0 & 0 & -a_{w,4} & 0 & 0 & a_{p,7} & -a_{t,7} & 0 \\ 0 & 0 & 0 & 0 & -a_{w,5} & 0 & -a_{b,8} & a_{p,8} & -a_{t,8} \\ 0 & 0 & 0 & 0 & 0 & -a_{w,6} & 0 & -a_{b,9} & a_{p,9} \end{pmatrix} \begin{Bmatrix} P_1 \\ P_2 \\ P_3 \\ P_4 \\ P_5 \\ P_6 \\ P_7 \\ P_8 \\ P_9 \end{Bmatrix} = \begin{Bmatrix} b_1 \\ b_2 \\ b_3 \\ b_4 \\ b_5 \\ b_6 \\ b_7 \\ b_8 \\ b_9 \end{Bmatrix} \tag{9}$$

The elimination process (forward substitution) is divided into two steps:

(Step A)

(1) Eliminate second row's first column pivot by the first row equaiton.
(2) Eliminate third row's second column pivot by the second row equation.

(Step B)

(1) Eliminate fourth row's first column pivot by the first row equation.
(2) Eliminate fourth row's second column pivot by the second row equation.
(3) Eliminate fourth row's third column pivot by the third row equation.

(Continue (1)–(3) processes for fifth to ninth rows.)

The resulting equation is shown in Eq. (10), where the coefficients A and B are obtained from steps (A) and (B) and is solved by backward substitution. Zero terms are ignored to reduce the operation count, and the Reynolds cavitation boundary condition [6] is imposed during the backward substitution process.

Table 2 provides the programming logic for application to a large number of CVs. The examples in Sec. 6 confirm the highly significant time savings achieved by the aforementioned algorithm as applied to calculating the bearing's dynamic coefficients. Part II

Table 2 General expression of proposed solver for discretized Reynolds equation

Step A for $I = 2 : N_K$ eliminate Ith row's $(I-1)$th column pivot by $(I-1)$th row eq.
Step B for $I = N_K + 1 : N_I N_K$ for $J = 1 : N_K$ eliminate Ith row's $(I + J - N_K - 1)$th column pivot by $(I + J - N_K - 1)$ th row eq.

Note: N_I: element number in x direction and N_K: element number in z direction.

shows a similar benefit when applied to the ME.

$$\begin{matrix} \\ Step\,A \\ \\ \downarrow \\ \\ Step\,B \\ \\ \\ \\ \\ \end{matrix} \begin{pmatrix} A_{1,1} & A_{2,1} & A_{3,1} & A_{4,1} & 0 & 0 & 0 & 0 & 0 \\ 0 & A_{1,2} & A_{2,2} & A_{3,2} & A_{4,2} & 0 & 0 & 0 & 0 \\ 0 & 0 & A_{1,3} & A_{2,3} & A_{3,3} & A_{4,3} & 0 & 0 & 0 \\ 0 & 0 & 0 & B_{1,4} & B_{2,4} & B_{3,4} & B_{4,4} & 0 & 0 \\ 0 & 0 & 0 & 0 & B_{1,5} & B_{2,5} & B_{3,5} & B_{4,5} & 0 \\ 0 & 0 & 0 & 0 & 0 & B_{1,6} & B_{2,6} & B_{3,6} & B_{4,6} \\ 0 & 0 & 0 & 0 & 0 & 0 & B_{1,7} & B_{2,7} & B_{3,7} \\ 0 & 0 & 0 & 0 & 0 & 0 & 0 & B_{1,8} & B_{2,8} \\ 0 & 0 & 0 & 0 & 0 & 0 & 0 & 0 & B_{1,9} \end{pmatrix}$$

$$\times \begin{Bmatrix} P_1 \\ P_2 \\ P_3 \\ P_4 \\ P_5 \\ P_6 \\ P_7 \\ P_8 \\ P_9 \end{Bmatrix} = \begin{Bmatrix} A_{5,1} \\ A_{5,2} \\ A_{5,3} \\ B_{5,4} \\ B_{5,5} \\ B_{5,6} \\ B_{5,7} \\ B_{5,8} \\ B_{5,9} \end{Bmatrix} \tag{10}$$

MATLAB sparse matrix codes are applied in the FVM solution of the between pad, 3D fluid domains. However, the 2D film domain modeled with the Reynolds equation results in a relatively small K matrix, compared with the 3D domains, eliminating the advantage of sparse matrix solvers over the proposed direct solver.

In addition, the sparse matrix approach requires time for an additional global assembly process and transformation to the sparse matrix form. Thus, the direct solver is applied in the film domain, and a sparse matrix solver is applied in all other domains.

2.2.2 Hybrid Between Pad Model. The groove region between pads is divided into a 1D OBP and a 3D IBP model. The combined model is referred to as a HBP model. The solution of the HBP model is continuously updated with modification of the interface boundary during the time integration of the dynamic rotor-pad solver, as described in Sec. 3. In this manner, mass and energy continuity at the interface is maintained in the final converged solution. Figure 3 illustrates the IBP and OBP parts of the HBP model. The 2D flow velocity fields at the IBP inlet and outlet are set equal to the Reynolds equation values for the fluid film. There are two contributions to the radial flow in the IBP. The first is the classical "makeup" flow component, which represents the difference between the preceding pad's trailing-edge output flow and the following pad's leading-edge input flow. The second contribution is from the "penetrating" flow, which is obtained from the machine learning output. The makeup flow is present for all cases, with or without the penetrating flow. The same amount of the penetrating flow enters and exits the IBP; therefore, mass is always conserved for both with and without penetrating flow cases. Conclusively, the mass flow is conserved for the IBP domain. The assumption is justified since the flow in the IBP is nearly laminar and without a pressure gradient in the axial (z) direction.

The 3D energy Eq. (6) is applied to the IBP to obtain the IBP temperature distribution. This simplified model for the IBP flow provides an efficient and accurate solution in the IBP domain. Note that the IBP flow and temperature are not directly affected by the fresh supply oil injection at this point in the solution procedure.

Figure 4 illustrates the mass and heat flows in the OBP domain. A complete mixing assumption is applied in the radial and circumferential directions, and the CVs are axially divided to account for the temperature distribution by the OBP inlet and side end effects [23]. The OBP temperature is calculated from the heat balance in the following equation:

$$q_{trans,(k)} = q_{in,(k)} - q_{out,(k)} + q_{sup,(k)} + q_{conv,(k)} + q_{cond,(k)} \tag{11}$$

where

$$\begin{cases} q_{sup,(k)} = \rho_f C_{p,f} Q_{sup,(k)} T_{sup} \\ q_{in,(k)} = \rho_f C_{p,f} (\max[Q_{in,(k)}, 0]\, T_{OB,(k-1)} - \max[-Q_{in,(k)}, 0]\, T_{OB,(k)}) \\ q_{out,(k)} = \rho_f C_{p,f} (\max[Q_{out,(k)}, 0]\, T_{OB,(k)} - \max[-Q_{out,(k)}, 0]\, T_{OB,(k+1)}) \\ q_{conv,(k)} = \rho_f C_{p,f} \sum_{i=1}^{N_{IBI}} (\max[Q_{conv,(i,1,k)}, 0]\, T_{IB,(i,1,k)} - \max[-Q_{conv,(i,1,k)}, 0]\, T_{OB,(k)}) \\ q_{cond,(k)} = \sum_{i=1}^{N_{IBI}} \{2k_f \Delta x \Delta z / \Delta y \times (T_{IB,(i,1,k)} - T_{OB,(k)})\} \\ q_{trans,(k)} = \rho_f V_{OB} C_{p,f} \dot{T}_{OB,(k)} \end{cases} \tag{12}$$

where T_{IB} and T_{OB} are the IBP and OBP fluid temperatures, respectively, and T_{sup} is the supply oil temperature. The subscript (k) is the OBP CV index in the axial direction. The subscripts (i, j, k) indicate the IBP CV index in the circumferential, radial, and axial directions, respectively. The subscript $(i, 1, k)$ is the index of the IBP CV that is contacted with the OBP CV, as shown in Fig. 4. The term N_{IBI} denotes the number of circumferential CVs in the OBP, and Q_{sup} is the supply oil flowrate obtained from the ML, as described in Sec. 2.2.3. The supply oil flow is only applied at the OBP inlet (mid-span CVs) as represented in Fig. 3, and by symmetry half, the amount of the supply oil flows out of both side outlets. Axial flows Q_{in} and Q_{out} are determined from the mass balance, as shown in Fig. 4(*a*).

The HBP model consists of the IBP and OBP models. The global mass matrix, stiffness matrix, and force vector of the HBP are obtained by combining the discretized equations of Eq. (6) on the IBP and heat balance equations of Eq. (11) on the OBP. Thus, the global M, K, and F form of the HBP can be expressed as follows:

$$\underset{(N_{BP}\times N_{BP})}{[M_{BP}]}\ \underset{(N_{BP}\times 1)}{\{\dot{T}_{BP}\}} + \underset{(N_{BP}\times N_{BP})}{[K_{BP}]}\ \underset{(N_{BP}\times 1)}{\{T_{BP}\}} = \underset{(N_{BP}\times 1)}{\{F_{BP}\}} \tag{13}$$

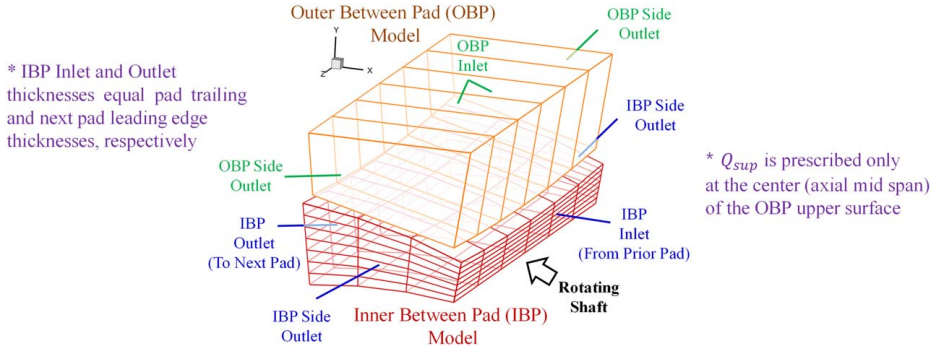

Fig. 3 Outer and inner layers of the HBP model

The dependent variables of the HBP model are contained in the vector:

$$\{T_{BP}\} = \{T_{IB,1}, \ldots, T_{IB,N_{IB}}, T_{OB,1}, \ldots, T_{OB,N_{OB}}\}^T \tag{14}$$

where N_{BP} is the number of the HBP's total CVs, and it is the summation of the IBP's total CVs (N_{IB}) and OBP's total CVs (N_{OB}). Equation (13) is solved with a steady-state assumption in the static and dynamic coefficient solver, while a transient solution is conducted for the ME simulation. A fully implicit method is selected to solve Eq. (13) due to the stiff matrix, which requires considerable computation time in the HBP model. Equation (15) is derived through the fully implicit method:

$$\underset{(N_{BP}\times N_{BP})}{[K^o_{BP}]}\ \underset{(N_{BP}\times 1)}{\{T_{BP}\}} = \underset{(N_{BP}\times 1)}{\{F^o_{BP}\}} \tag{15}$$

where $[K^o_{BP}] = [M_{BP}]/\Delta t + [K_{BP}]$, $\{F^o_{BP}\} = \{F_{BP}\} + [M_{BP}]\{T^o_{BP}\}/\Delta t$, where Δt is the time-step that corresponds to the update period of the fluid film energy equation, and $\{T^o_{BP}\}$ is the HBP temperature vector at the previous time-step. Equations (7), (8), and (15) are solved separately for each pad. However, the temperature and the pressure of each interface are continuously updated in the time domain.

2.2.3 Machine Learning Axial Mixing Coefficient. Yang and Palazzolo [23] demonstrated that MCs are actually distributions, as opposed to a single value, and vary in the axial direction, as shown in Fig. 5. This section provides a modeling method considering the axial MC distribution. The axial MC is defined as shown in Eq. (16). The overbar of $\bar{T}(z)$ indicates the mass flowrate weighted average temperature as shown in Eq. (17). As shown in Fig. 3, $\bar{T}_{IBP,out}$ is the temperature at the IBP outlet, and $\bar{T}_{IBP,in}$ is the temperature at the IBP inlet. T_{sup} is the oil supply temperature.

$$\eta(z) \equiv \frac{\bar{T}_{IBP,out}(z) - T_{\text{sup}}}{\bar{T}_{IBP,in}(z) - T_{\text{sup}}} \tag{16}$$

$$\bar{T}(z) = \frac{\int \rho_f u C_{p,f} T dr}{\int \rho_f u C_{p,f} dr} \tag{17}$$

The HBP model presented in Sec. 2.2.2 ignores the concentrated supply flow that penetrates the IBP and axial flows. Thus, the resulting "original" axially distributed mixing coefficient (AMC) $\eta_0(z)$ are inaccurate near the oil inlet and pad edges, but very accurate in the intermediate regions. ML is utilized to predict the axial MC, which combines with the HBP solution. Here, ML acts as a regression model for the axial MC, and the axial MC $\eta_{nn,0}(z)$ predicted by the ML are called the "original neural network axial mixing coefficient (NNAMC)" in this study. The details of the methodology for a related ML algorithm were provided in Ref. [23]. This treated the MC as a single area-averaged value. One novel contribution of the present work is to include the axial MC effect via the neural network (NN) of the ML.

The overall methodology sequence for obtaining the trained NN is represented in Fig. 6(*a*). First, input parameter sets are obtained from a combination of the Latin hypercube sampling and full factorial design of experiment (DOE) methods [23]. Figure 7 shows the DOE parameters (ML inputs), and Table 3 lists the parameters and their bounds. Second, CFD simulations are performed for the groove between pad domains for all DOE-generated parameter sets. Third, the axial MC results from the CFD simulations are utilized for training and validating the axial MC NN. Finally, as shown in Fig. 6(*b*), the trained NNAMC, represented by $\eta_{nn,0}(z)$, are combined with the original HBP model's MC. The original AMC $\eta_0(z)$ of the HBP model is corrected to consider the nozzle and side end effects utilizing a corrected form $\eta_{nn,c}(z)$ of the $\eta_{nn,0}(z)$, and the result is referred to as the MLAMC $\eta_{ml}(z)$. The MLAMC is utilized to determine an equivalent oil supply injected flow distribution Q_{pnt}, which penetrates the IBP. This distribution is searched for iteratively until the mixing coefficients evaluated from the HBP domain model become equal to the $\eta_{ml}(z)$. Convergence of this iterative procedure yields the IBP outlet temperature, which is the desired radially and axially varying temperature distribution imposed on the pad's fluid film's energy equation solution.

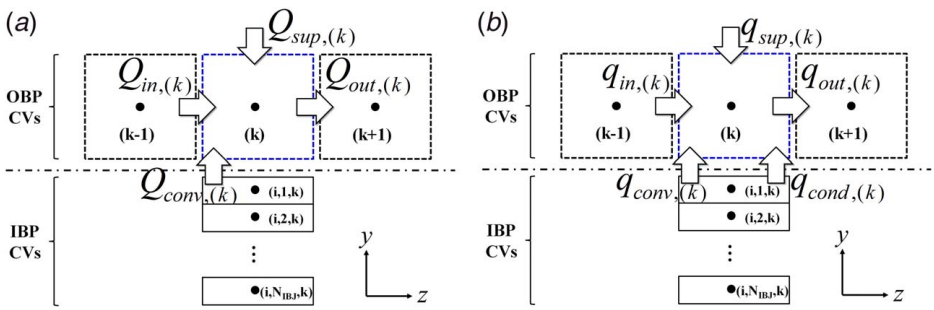

Fig. 4 Mass and heat balances of OBP model for a control volume: (*a*) mass balance and (*b*) heat balance

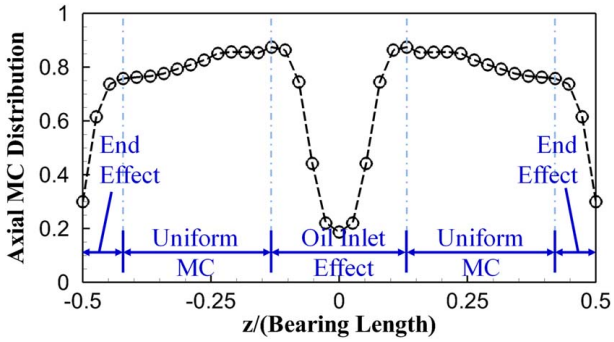

Fig. 5 Axial MC distribution for BP with a central oil inlet [23]

The NN consists of layers and neurons as illustrated in Fig. 8. This represents the designed NN for the axial MC regression. Important input parameters ($n_i = 9$) are chosen from sensitivity analyses [23], and ten output neurons ($n_o = 10$) are employed. Only one hidden layer is involved in the NN, and the number of neurons in the hidden layer ($n_j = 50$) is determined from the best performance case over several simulations.

Each output neuron builds the NNAMC, according to axial direction locations, as illustrated in Fig. 8. The NNAMC outputs of the trained NN can be calculated after the input parameters transfer through the neurons of the hidden and output layers, according to the neuron's connections shown in Fig. 8. Equation (18) represents the relation of the neuron's inputs ($y^k_{j,i}$) and output (Y^k_j) by the hyperbolic tangent activation function, weighting factors, and bias factors (i: neuron's input index, j: neuron index, and k: layer index).

$$Y^k_j = \tanh\left(\sum_{i=1}^{n_i} w^k_{j,i} y^k_{j,i} + w^k_{j,0}\right) \tag{18}$$

The weighting and bias factors ($w^k_{j,i}$, $w^k_{j,0}$) are saved in the NN through the training process.

The HBP model can be enhanced to more accurately predict the fluid film leading-edge temperature near an oil nozzle inlet and near the axial ends in Fig. 5. The flow that penetrates into the IBP region [20,22–25] must be included in the HBP model. The equivalent penetrating flow ($Q_{pnt,k}$) is introduced for this purpose, as represented in Fig. 9. The flow penetrating from the OBP to the IBP CVs is $Q_{pnt,k}$, which distributes equally toward both the leading and trailing edges. For more than three CVs in the circumferential direction, the backflow from IBP to OBP is only applied in the leading and trailing-edge CVs. All CV original flowrates are calculated by mass balance without $Q_{pnt,k}$, and the original flowrate is summed with the penetrating flow. The penetrating flow ($Q_{pnt,k}$) is assumed to flow circumferentially and radially uniformly because the IBP is very thin. The criterion for determining the penetrating flow distribution is that it must produce a temperature distribution at the IBP outlet and corresponding axial mixing coefficients that match the previously determined $\eta_{ml}(z)$. The penetrating flow distribution is calculated from the Newton–Raphson procedure shown in Eq. (19).

$$\begin{Bmatrix} Q^{new}_{pnt,1} \\ Q^{new}_{pnt,2} \\ \vdots \\ Q^{new}_{pnt,n_{IBK}} \end{Bmatrix} = \begin{Bmatrix} Q^{old}_{pnt,1} \\ Q^{old}_{pnt,2} \\ \vdots \\ Q^{old}_{pnt,n_{IBK}} \end{Bmatrix} - \begin{bmatrix} \frac{d\eta_1}{dQ_{pnt,1}} & \frac{d\eta_1}{dQ_{pnt,2}} & \cdots & \frac{d\eta_1}{dQ_{pnt,n_{IBK}}} \\ \frac{d\eta_2}{dQ_{pnt,1}} & \frac{d\eta_2}{dQ_{pnt,2}} & \cdots & \frac{d\eta_2}{dQ_{pnt,n_{IBK}}} \\ \vdots & \vdots & \ddots & \vdots \\ \frac{d\eta_{n_{IBK}}}{dQ_{pnt,1}} & \frac{d\eta_{n_{IBK}}}{dQ_{pnt,2}} & \cdots & \frac{d\eta_{n_{IBK}}}{dQ_{pnt,n_{IBK}}} \end{bmatrix}^{-1} \begin{Bmatrix} \eta_1 - \eta_{ml,1} \\ \eta_2 - \eta_{ml,2} \\ \vdots \\ \eta_{n_{IBK}} - \eta_{ml,n_{IBK}} \end{Bmatrix} \tag{19}$$

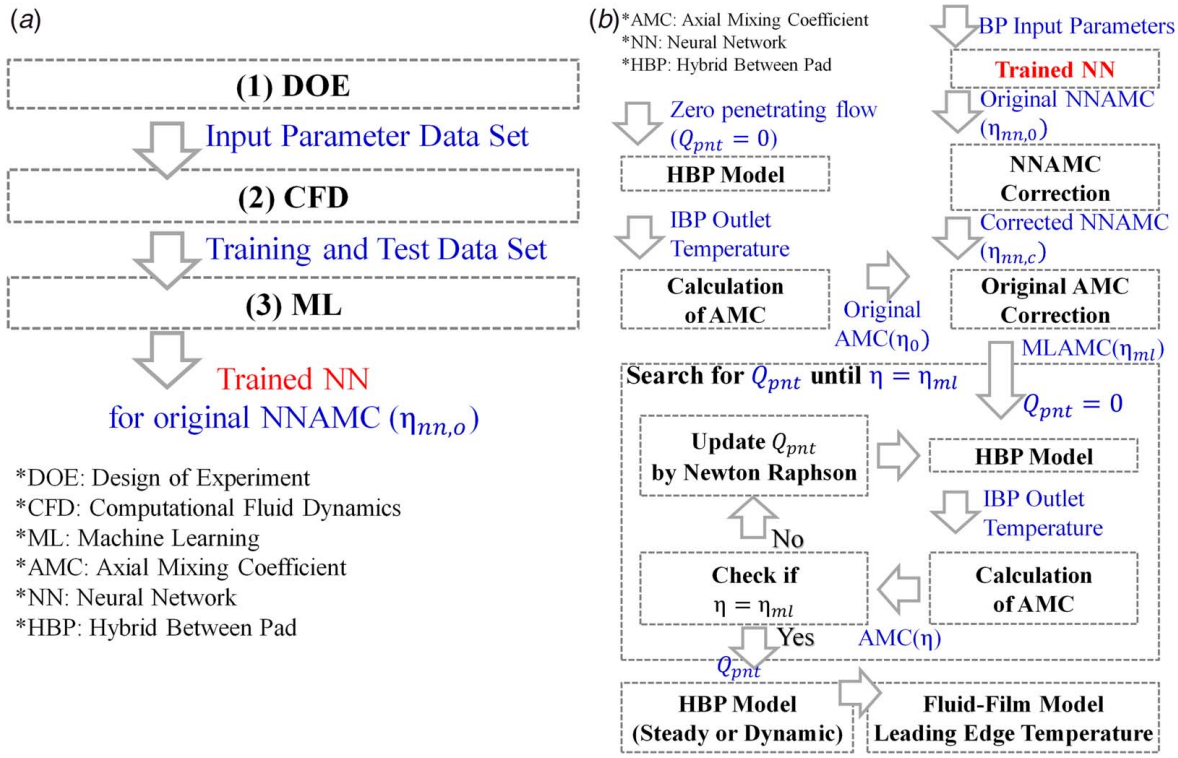

Fig. 6 Flow diagram for obtaining axial and radial varying temperature distribution at a pad leading edge: (*a*) trained NN and (*b*) application of trained NN for obtaining fluid-film leading-edge temperature distribution

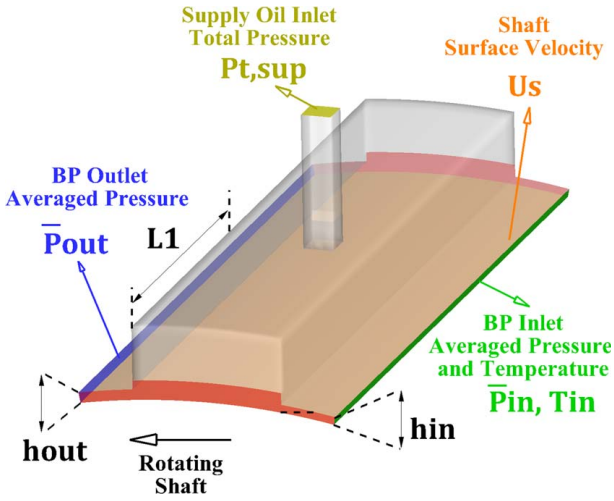

Fig. 7 Illustration of input parameters for machine learning [23]

Table 3 Input parameters and the bounds for machine learning [23]

Parameters	Min value	Max value	Unit
(1) L_1/R_s	0.4	1.0	–
(2) R_s	25.4	76.2	mm
(3) T_{in}	50	120	°C
(4) U_s	15	95	m/s
(5) $P_{t,sup}$	0.01	0.7	MPag
(6) $\overline{P}_{in}$	0	1.2	MPag
(7) $\overline{P}_{out}$	0	0.65	MPag
(8) $h_{in}/C_{l,b}$	0.3	2.2	–
(9) $h_{out}/C_{l,b}$	0.3	2.2	–

Note: R_s: shaft radius.

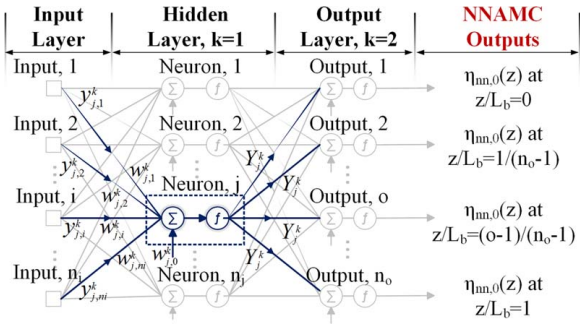

Fig. 8 Neural network for axial MC regression

where η_k is the axial MC calculated from the HBP model during the Newton–Raphson iteration, k is the axial CV index, Q_{pnt} is the penetrating flow to be solved for, and n_{IBK} is the number of CV layers in the axial direction.

The Newton–Raphson iteration in Eq. (19) requires a high computational load since the iteration process is nested in the time integration solver. The penetrating flow iteration scheme is implemented only near the oil inlet and side end regions to reduce computation time. This is a reasonable assumption because the equivalent penetrating flow is absent in the uniform MC region [23] as shown in Fig. 5.

Therefore, the HBP model, without penetrating flow, has sufficient accuracy in the uniform MC region. The MLAMC is defined in Eq. (20) and is illustrated in Fig. 10.

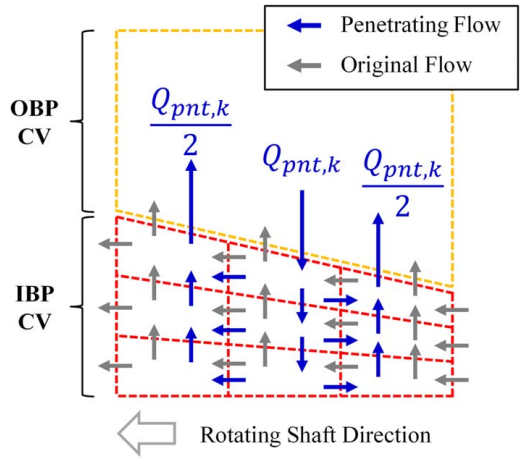

Fig. 9 Addition of IBP penetrating flow $Q_{pnt,k}$ to replicate $\eta_{ml}(z)$ near the oil inlet and side end edges

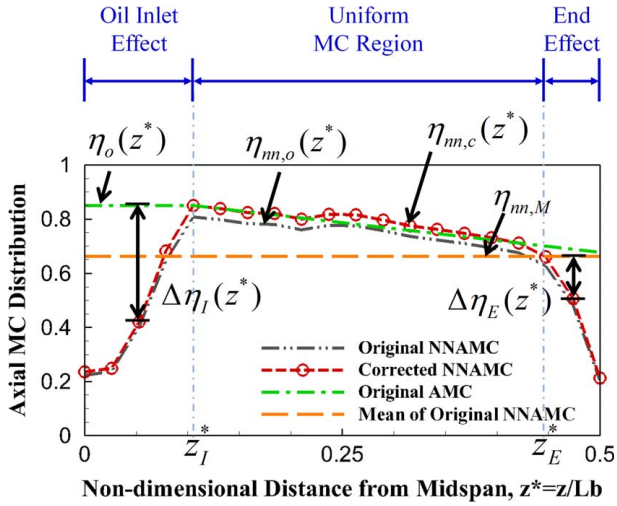

Fig. 10 Mixing coefficient distributions $\eta_0(z)$, $\eta_{nn,0}(z)$ and $\eta_{nn,c}(z)$, mean of $\eta_{nn,0}(z)$, and oil inlet, uniform and end effect axial regions

MLAMC distribution is expressed as follows:

$$\eta_{ml}(z) = \begin{cases} \eta_0(z^*) - \Delta\eta_I(z^*), & 0 \le z^* \le z_I^* \\ \eta_0(z^*), & z_I^* \le z^* \le z_E^* \\ \eta_0(z^*) - \Delta\eta_E(z^*), & z_E^* \le z^* \le 0.5 \end{cases} \tag{20}$$

where z^* is the nondimensional distance along the bearing length from the mid-span, η_0 is the original axial MC taken from the HBP model when there is no penetrating flow, and z_I^* is the location where the slope of the original NNAMC ($\eta_{nn,0}$) changes from positive to negative. The oil inlet region is defined from 0 to z_I^*. The location z_E^* is where $\eta_{nn,0}$ becomes less than the mean of the original NNAMC ($\eta_{nn,M}$), where $\eta_{nn,0}$ is the axial MC predicted from the NN without any corrections. The side end region is defined from z_E^* to 0.5. As shown in Eq. (21), $\eta_{nn,0}$ is modified to become the corrected NNAMC $\eta_{nn,\,c}(z)$. This correction is performed to ensure similarity of the MC between the HBP and NN models in the uniform MC region.

$$\eta_{nn,c}(z^*) = \frac{\eta_0(z_I^*)}{\eta_{nn,0}(z_I^*)}\eta_{nn,0}(z^*) \tag{21}$$

The similarity is justified since there is no penetrating flow in the uniform MC region. The main heat transfer mechanism in the

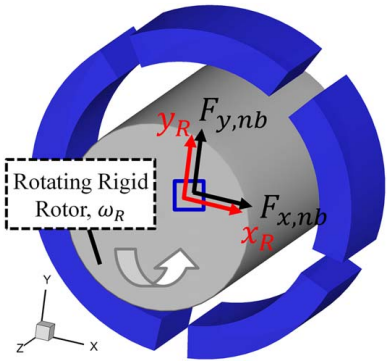

Fig. 11 Degrees-of-freedom of the rigid rotor model with applied force

uniform MC region is the inflow of makeup cold oil from the OBP region and thermal diffusion. Thus, if the penetrating flow (strong convection) occurs in the uniform MC region, it would yield an overcooled shaft surface temperature. Equation (20), including the definition in Eq. (21), is substituted into Eq. (19). The original axial MC in the HBP model is corrected by the $\Delta\eta_I$ near the oil inlet region ($0 \le z^* \le z_I^*$) and by $\Delta\eta_E$ near the side end region ($z_E^* \le z \le 0.5$). The quantities $\Delta\eta_I$ and $\Delta\eta_E$ are the axial MC changes due to the cooling effect of the penetrating flow and are evaluated from the following equations:

$$\Delta\eta_I(z^*) = \eta_0(z_I^*) - \eta_{nn,c}(z^*) \tag{22}$$

$$\Delta\eta_E(z^*) = \eta_{nn,M} - \eta_{nn,c}(z^*) \tag{23}$$

The MLAMC in Eq. (20) provides the mixing coefficient MC distribution along the axial direction of the half bearing. In practice, $\Delta\eta_I$ and $\Delta\eta_E$ are symmetrically applied to the full bearing. In addition to the NN ML of the axial MC (NN-Axial MC), the NN ML [23] is also applied for prescribing the pressure boundary conditions of the Reynolds model at the pad leading and trailing edges. Finally, NN ML is also applied to the drag torque and supply flowrate [23] bearing outputs. The total supply pressure is one of the input parameters in all NNs, including the NN-axial MC, NN-pressure, and NN-drag torque and supply flowrate. In this study, the supply flowrate is an input condition. Thus, the total supply pressure for all NNs is iteratively updated until the supply flowrate predicted from the NN-drag torque and supply flowrate is identical to the given supply flowrate. An in-depth description of this process is provided in Ref. [23].

2.3 Dynamic Rotor and Pad Model. The rotor is treated as a rigid mass m_R in a transient search for the equilibrium position, about which the linearized bearing force coefficients are evaluated. Figure 11 shows the x and y degrees-of-freedom (DOFs) of the rotor, and the components of the resultant integrated pressure force plus external applied load. The rotor equation is expressed as follows:

$$\underset{(2\times2)}{[M_R]}\ \underset{(2\times1)}{\{\ddot{x}_R\}} = \underset{(2\times1)}{\{F_R\}} \tag{24}$$

where $[M_R]$ is the rotor's mass matrix with rotor mass m_R, $\{F_R\}$ is the rotor's force vector with components $\{F_{x,nb}, F_{y,nb}\}^T$, and $\{x_R\}$ equals $\{x_R, y_R\}^T$, as shown in Fig. 11.

Figure 12 shows the rigid and flexible pad models, along with the associated DOFs and applied forces. The nonlinear pivot stiffness k_{pvt}^j, based on Hertzian contact theory [7] is included with both pad models. Pivot flexibility decreases dynamic coefficients and damping ratios as demonstrated in Ref. [21].

The pad includes a 0.5 offset, and the cylindrical pivot allows only tilting and pivot (radial) motions. The pad dynamical equations are expressed as follows:

Rigid pad:

$$M_{PG}^j \ddot{x}_{pvt}^j + k_{pvt}^j x_{pvt}^j = \sum_i (F_{nx,i}^j + F_{tx,i}^j) \tag{25}$$

$$I_G^j \ddot{\delta}_{tilt}^j = \sum_i (M_{n,i}^j + M_{t,i}^j) \tag{26}$$

Flexible pad:

$$\underset{(3n_p^j\times3n_p^j)}{[M_p^j]}\ \underset{(3n_p^j\times1)}{\{\ddot{x}_p^j\}} + \underset{(3n_p^j\times3n_p^j)}{[K_p^j]}\ \underset{(3n_p^j\times1)}{\{x_p^j\}} = \underset{(3n_p^j\times1)}{\{F_p^j\}} \tag{27}$$

where M_{PG}^j and I_G^j are the jth pad's mass and mass moment of inertia, respectively, $F_{nx,i}^j$ and $F_{tx,i}^j$ indicate the x-direction forces (local coordinate) from the normal and tangential forces ($F_{n,i}^j$ and $F_{t,i}^j$) on the pad surface, and the moments ($M_{n,i}^j$ and $M_{t,i}^j$) are determined from the normal and tangential forces, respectively, where the forces are calculated from the solution of the Reynolds equation. The terms $[M_p^j]$, $[K_p^j]$, and $[F_p^j]$ are the mass matrix, stiffness matrix, and force vector of the jth pad and are derived based on the 3D structural FEM [27] as given in "Three-Dimensional Finite Element Method Matrix for Structure Deformation (3D Hexahedron Element, Three Degrees-of-Freedom for 1 Node)" in the Appendix. The term n_p^j is the total node number of the jth pad, and each node has 3DOFs, as shown in Fig. 12(*b*).

A modal reduction technique is applied to the pad dynamic model to reduce computation time. Equation (28) is the jth pad's motion equation in modal coordinates $\{\xi_p^j\}$. The pad's eigenvalue matrix $[\lambda_p^j]$, modal mass matrix $[M_{\xi,p}^j]$, and modal force vector $\{F_{\xi,p}^j\}$ are given in Eqs. (29)–(31), where $[\Phi_p^j]$ is the pad eigenvector matrix with m_p modes. Pad dynamics are solved simultaneously with the

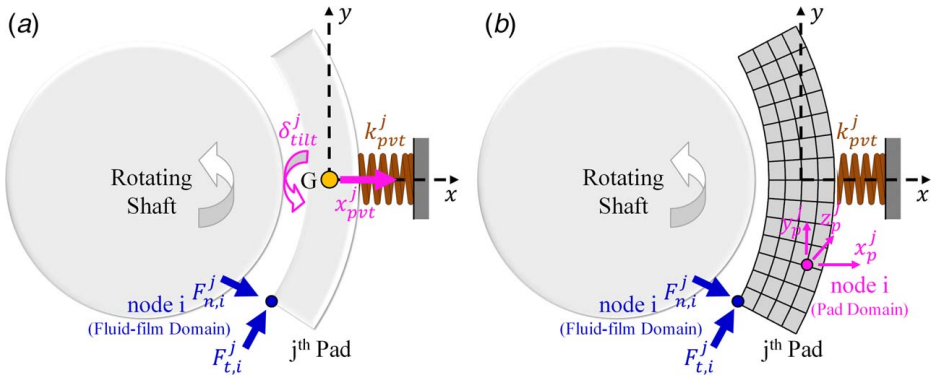

Fig. 12 Pad dynamics models with a flexible pivot: (*a*) rigid pad and (*b*) flexible pad (*j*: pad index and *i*: node index in fluid film domain)

rotor dynamics.

$$\underset{(m_p\times 1)}{\{\ddot{\xi}_p^j\}} + \underset{(m_p\times m_p)}{[\lambda_p]}\ \underset{(m_p\times 1)}{\{\xi_p^j\}} = \underset{(m_p\times m_p)}{[M_{\xi,p}]^{-1}}\ \underset{(m_p\times 1)}{\{F_{\xi,p}\}} \tag{28}$$

$$\underset{(m_p\times m_p)}{[\lambda_p^j]} = \underset{(m_p\times 3n_p^j)}{[\Phi_p^j]^T}\ \underset{(3n_p^j\times 3n_p^j)}{[M_p^j]^{-1}}\ \underset{(3n_p^j\times 3n_p)}{[K_p^j]}\ \underset{(3n_p^j\times m_p)}{[\Phi_p^j]} \tag{29}$$

$$\underset{(m_p\times m_p)}{[M_{\xi,p}^j]} = \underset{(m_p\times 3n_p^j)}{[\Phi_p^j]^T}\ \underset{(3n_p^j\times 3n_p^j)}{[M_p^j]}\ \underset{(3n_p^j\times m_p)}{[\Phi_p^j]} \tag{30}$$

$$\underset{(m_p\times 1)}{\{F_{\xi,p}^j\}} = \underset{(m_p\times 3n_p^j)}{[\Phi_p^j]^T}\ \underset{(3n_p^j\times 1)}{\{F_p^j\}} \tag{31}$$

2.4 Steady-State Thermal Rotor and Pad Model. Figure 13 shows the finite element pad domains with five pads and finite element shaft domain. The latter includes solid elements in the journal region and beam elements for the remainder of the shaft. These two submodels for the shaft are connected by fictitious, rigid massless beam elements. The shaft temperature distribution in the region of the journal is assumed axisymmetric for calculating the bearing's dynamic coefficients. It has a general asymmetric form when calculating ME response, where synchronous vibration in the bearing due to imbalance and thermal rotor bow causes temperature asymmetry. The combined solid element–beam element model is essential for ME simulations to obtain accurate journal temperature distributions, and internal bending moments, along with overall shaft vibration modeling. A detailed related discussion is presented in Part II.

The temperature in the solid domains (pads and shaft) are obtained via FEM solution of the steady-state heat conduction equation:

$$\nabla \cdot (k_s \nabla T_s) = 0 \tag{32}$$

where s is the solid domain subscript for the shaft and pads, k_s is the solid thermal conductivity, and T_s is the solid's temperature. The FEM discretized form [28] of the heat conduction equation, as presented in "Discretized Equation for Three-Dimensional Energy Equation in Fluid (3D Hexahedron Element)" in the Appendix is expressed as follows:

$$\underset{(n_{T,s}\times n_{T,s})}{[K_{T,s}]}\ \underset{(n_{T,s}\times 1)}{\{T_s\}} = \underset{(n_{T,s}\times 1)}{\{F_{T,s}\}} \tag{33}$$

where the stiffness matrix and force vector of heat conduction are $[K_{T,s}]$ and $\{F_{T,s}\}$, respectively, and $n_{T,s}$ indicates the number of nodes of the solid domain. The solid's temperature solutions $\{T_s\}$ in Eq. (33) are substituted into the thermal load terms $\{F_s\}$ in Eq. (34) to obtain the thermal deformation total displacements $\{x_{t\ s}\}$. The stiffness matrix $[K_s]$ and force vector $\{F_s\}$ for the thermal deformation are obtained based on FEM, as described in (A3). The number of nodes is n_s for the solid domain for the thermal deformation.

$$\underset{(3n_s\times 3n_s)}{[K_s]}\ \underset{(3n_s\times 1)}{\{x_{t\ s}\}} = \underset{(3n_s\times 1)}{\{F_s\}} \tag{34}$$

2.5 Dynamic Coefficient. A detailed description for obtaining the dynamic coefficients is briefly presented here and presented in more detail in Refs. [21,22]. The dynamic coefficients ($\boldsymbol{k}_{brg}$, $\boldsymbol{c}_{brg}$) are condensed from the full dynamic coefficients ($\boldsymbol{k}_{fbrg}$, $\boldsymbol{c}_{fbrg}$). The condensed dynamic coefficients are referred to as synchronously reduced dynamic coefficients. Also, log decrements in Eq. (35) are computed to evaluate the stability of the rotor-bearing system with the rigid rotor supported by two symmetric TPJBs [21]:

$$\delta_{d,i} = \frac{2\pi\varphi_i}{\sqrt{1-\varphi_i^2}} \tag{35}$$

where $\varphi_i = -real(\lambda_{r,i})/|\lambda_{r,i}|$, and $\lambda_{r,i}$ are the rotor-bearing system eigenvalues.

2.6 Boundary Condition. Imposing the correct natural and essential boundary conditions is critical for numerically solving this multiphysics boundary value problem. This section discusses the boundary conditions for all interfaces in the computational domains. Figure 14 depicts the prescribed boundary conditions, and the information on the numberings (1)–(15) is explained in Table 4. The fluid-type domains consist of the HBP and fluid film domains, as shown in Figs. 14(*a*) and 14(*b*). As explained in Sec. 2.2.3, mass flowrate and temperature are imposed at the supply oil inlet (1), and the flowrate affects the pressure at the fluid film inlet (6) and outlet (7). The pressures are obtained from the pressure NN. The interfaces (3)–(7)^p and (4)–(6) take the identical velocity and temperature field at each interface (superscript p: for prior pad).

The OBP side outlet (2) is the opening boundary in which mass flowrate and temperature are calculated from the mass and heat balances. As discussed in Sec. 2.2.2, the IBP side outlet (5) is assumed to have zero flow. The side outlet temperatures of the IBP (5) and fluid film (8) are imposed as ambient temperature, and zero pressure is applied to the fluid-film side outlet (8). The solid's outer surfaces,

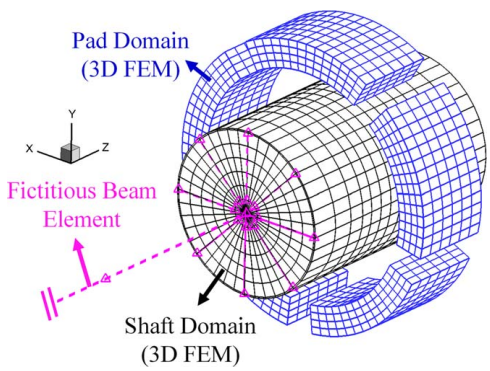

Fig. 13 Solid domains for temperature and thermal deformation predictions (dynamic coefficient solver)

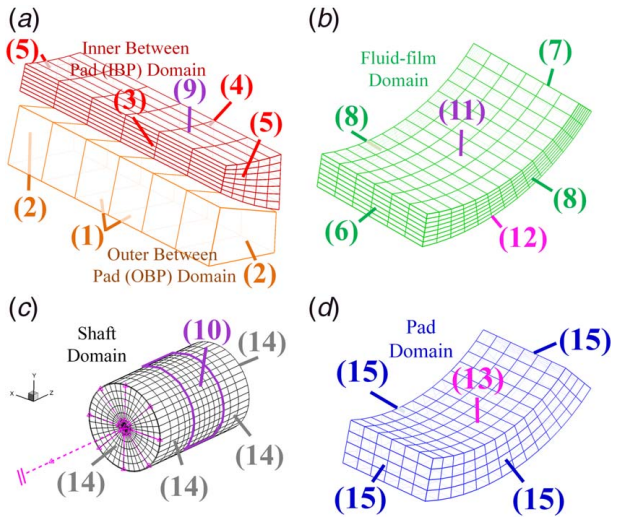

Fig. 14 Boundary conditions of the computational domains: (*a*) HBP, (*b*) fluid film, (*c*) shaft, and (*d*) pad

Table 4 Summary of prescribed boundary conditions in computational domains

No.	Description	Governing equation	B.C type
(1)	Supply oil inlet	Mass	Mass flow rate
		Energy	Temperature
(2)	OBP side outlet	Mass and energy	Opening
(3)	IBP inlet	Mass and energy	(3)–$(7)^p$ interface
(4)	IBP outlet	Mass and energy	(4)–(6) interface
(5)	IBP side outlet	Mass	Zero flow
		Energy	Temperature
(6)	Fluid-film inlet	Reynolds	Pressure (NN-P)
		Energy	(4)–(6) interface
(7)	Fluid-film outlet	Reynolds	Pressure (NN-P)
		Energy	$(3)^n$–(7) interface
(8)	Fluid-film side outlet	Reynolds	Pressure
		Energy	Temperature
(9)–(10)	IBP–shaft interface	Energy	$(9)^a$–(10) interface
(10)–(11)	Shaft–Fluid film interface	Energy	(10)–$(11)^a$ interface
(12)–(13)	Fluid film–pad interface	Energy	(12)–(13) interface
(14)	Shaft outer surface	Energy	HCC and temperature
(15)	Pad outer surface	Energy	HCC and temperature

Note: Superscripts: n: next pad; p: prior pad; a: all pads; interface: continuity of dependent variable; and HCC: heat convection coefficient.

(14) and (15), are prescribed with heat convection coefficients and temperatures. The interfaces (9)–(10), (10)–(11), and (12)–(13) between the fluid and solid domains are applied as in Eqs. (36) and (37).

$$k_f \left.\frac{\partial T_f}{\partial r}\right|_{(\theta,R_s,z)} = k_s \left.\frac{\partial T_s}{\partial r}\right|_{(\theta+\omega t,R_s,z)} \tag{36}$$

$$T_f|_{(\theta,R_s,z)} = T_s|_{(\theta+\omega t,R_s,z)} \tag{37}$$

where s is the solid domain index for the pad and shaft, and R_s is the radius at the interface. The shaft is modeled in the rotating frame, so the shaft's angular position θ_r in the rotating frame equals $\theta+\omega t$, where θ is the fixed frame angle. The shaft spin frequency ω is (ω_s), and the pad ω is zero in Eqs. (36) and (37). The shaft and pad interface temperatures are updated from the accumulated heat fluxes in Eq. (36) during one period of the spin frequency. In addition, the boundary conditions imposed for the structural analysis [7,20,29], including the dynamic and thermal deformation models, are provided in Fig. 15.

3 Algorithm for Static and Dynamic Coefficient Prediction

Figure 16 shows a flow diagram for determining TPJB dynamic coefficients, including the use of MLAMC for improving the pad inlet temperature distribution model. The main computation procedure is conducted in the dynamic rotor-pad solver, as illustrated in Fig. 16(*a*). The Reynolds, HBP, fluid-film energy, and dynamic model time integration solvers are coupled through the pressure (P), IBP temperature (T_{IB}), fluid film temperature (T_f), and rotor-pad displacements and velocity (Y_D). The pressures P are utilized to update fluid force terms on the rotor-pad model and to update velocity fields in the HBP and fluid film energy solvers. The temperatures T_{IB} and T_f are utilized for satisfying the fluid–fluid type interface boundary conditions between the IBP and the fluid film domains. The fluid-film energy solver continuously changes the dynamic viscosity field (μ_f) using the updated T_f. The motion variables Y_D affect the film thickness (h_f) and its time derivative ($\dot{h}_f$), which are used as parameters in all solvers of the fluid domains.

The dynamic rotor-pad solver sequentially computes the Reynolds, HBP, fluid-film energy, and dynamic model time integration solvers until the motion and thermal states have converged to steady-state equilibrium values [26]. The solid temperature fields (T_s) are obtained from the solid energy solver, after the motions have reached their steady-state equilibrium values. At that point, T_s is substituted into the thermal load term of the force vectors in the solid thermal deformation solver to obtain the total displacement vector by thermal deformation ($\mathbf{X}_{t\,s}$). This vector $\mathbf{X}_{t\,s}$ is then used to calculate the film thickness changes ($h_{s,TE}$) due to thermal expansion. The processes (2)–(4) continue until the temperature relative errors become acceptably small in all domains.

The synchronously reduced, dynamic coefficient solver (5) calculates the synchronously reduced dynamic coefficients, following T_s,

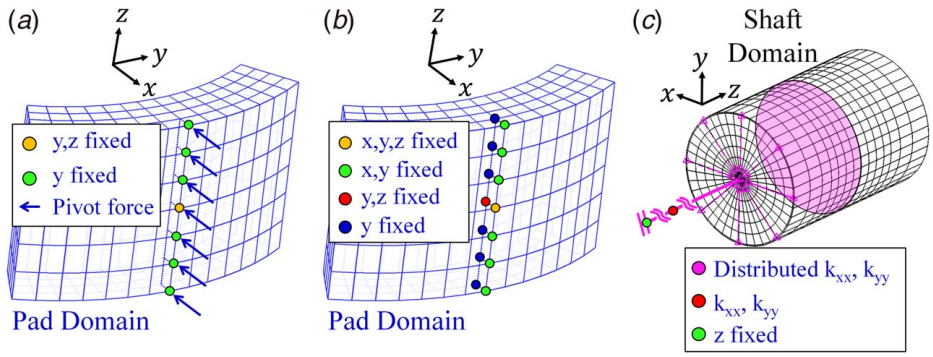

Fig. 15 Boundary conditions for structural analysis: (*a*) dynamic model (cylindrical pivot), (*b*) thermal deformation (cylindrical pivot), and (c) thermal deformation (shaft)

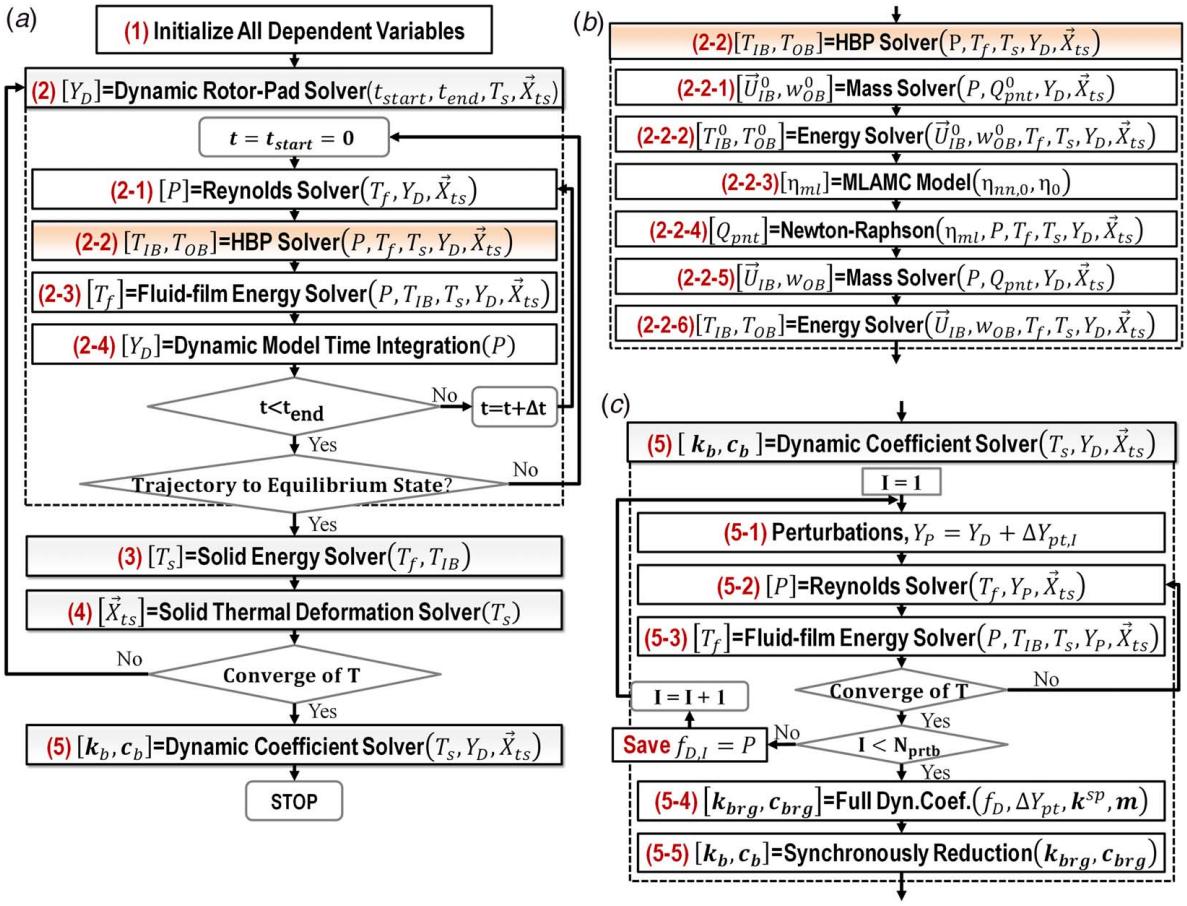

Fig. 16 Algorithm for static and dynamic coefficient prediction: (*a*) overall procedure, (*b*) HBP model solver, and (*c*) dynamic coefficient solver

Y_D, and $\mathbf{X}_{ts}$ reaching their steady-state equilibrium values. The detailed procedures of the dynamic coefficient solver by the perturbation method are given in Fig. 16(*c*). The author's prior study [21,22] elaborates on the dynamic coefficient calculation. Figure 16(*b*) shows the flow diagram for solving the HBP model including usage of the MLAMC to provide leading-edge, film temperature distributions. A comprehensive description of the HBP domain solution is provided in the companion Part II paper.

4 Comparison to Finite Element Method—Dynamic Coefficient Solver

Most bearing DC literature employ FEM solutions of the Reynolds and energy equations in the fluid-film domain, utilizing an upwind scheme for treating the convective term in the energy equation. A study is presented comparing solutions of the Reynolds and energy equations using the FEM and the FVM for solution accuracy and computational efficiency. The input parameters are selected from the author's prior study [22] for comparison and validation purposes. The input parameters are presented in Table 5, and they are applied identically for the FEM and FVM. The computational domains with these input values are illustrated in Fig. 17. The grid density was determined to be converged based on grid studies when considering the MLAMC, as derived from ten output neurons of the NN.

Figure 18 shows the fluid-film temperature fields at the Pad 1 mid-span for the FEM and FVM models. The results are obtained after the first 1/40 period of the spin frequency. The boundary temperature of the fluid film is assumed to be constant. The journal's operating speed is 9000 rpm, and the fluid-film leading-edge temperature is 60 °C. The pad surface temperature is 50 °C, and the shaft surface temperature is varied from 60 to 90 °C. The fluid-film leading-edge pressure in this section is constant, and its value is 132 kPa. Temperature discontinuities appear in the FEM solutions, as clearly shown in Fig. 18(*a*). This indicates that energy is not conserved near the discontinuity regions. This deficiency increases in

Table 5 Input parameters for static and dynamic coefficient prediction [22]

Parameters	Value
Shaft diameter (mm)	101.6
Bearing length (mm)	50.8
Bearing clearance (mm)	0.0749
Number of pads	5
Pad thickness (mm)	12.7
Pad thickness at pivot (mm)	15
Pad arc length (deg)	60
Pad offset	0.5
Applied load (N)	5000
Load direction	−Y
Preload	0.5
Operating speed (kRPM)	3–15
Pivot type	Rocker (cylindrical)
Load type	Load between pad
Outside HCC (W/m^{2}K)	50
Ambient temperature (°C)	30
Supply oil temperature (°C)	40
Selected pad flexible modes	1–20
Lubricant	ISO 32
Material (solid domains)	Steel

Note: HCC: heat convection coefficient.

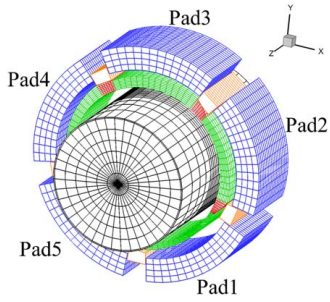

Fig. 17 Applied computational domains for static equilibrium and dynamic coefficient prediction (30,490 nodes, journal rotating direction: C.C.W.)

severity as the shaft surface temperature increases, as shown in Fig. 18(*a*). In contrast, the FVM shown in Fig. 18(*b*) does not show this deficiency since the discretization of the FVM strictly follows the conservation rules of transported quantities. The trailing-edge temperatures show close agreement between the FEM and FVM in spite of the temperature discontinuity in the FEM results.

Energy is approximately, globally conserved in the FEM approach, but is not locally conserved. FEM approaches in previous studies have generally yielded good results for static equilibrium quantities and dynamic coefficients. However, violations of local energy conservation with the FEM approach may lead to film temperature discontinuity near the shaft surface, which degrades the accuracy of the shaft temperature prediction. The shaft surface temperature is set equal to the film temperature at the node nearest to its shaft counterpart. Shaft temperature affects shaft thermal deformation, which in turn affects film thickness, which may have a considerable impact on static and dynamic coefficient results. The following section reveals that shaft temperature error, caused by the film temperature discontinuity problem, produces significant errors in the TPJB performance prediction.

The temperature discontinuity problem in the FEM approach is explained in the following discussion. Considering the energy equation, the FEM global stiffness matrix in Eq. (8) is obtained by summing (assembling) the element stiffness matrices ($[K^e_{T_f}]$):

$$[K^e_{T_f}] = \int_{\Omega^e} k_f \nabla W^e_i \cdot \nabla N^e_j d\Omega^e + \int_{\Omega^e} \rho_f C_{p,f} u^e_i \cdot \nabla N^e_j d\Omega^e \tag{38}$$

where W is a weight function, N is a shape function, and Ω indicates the element volume. The assembly procedure provides the following expression for the temperature at node p:

$$a_p T_p = \sum_{nb=i} a_{nb} T_{nb} + b_p \tag{39}$$

where nb indicates the neighbor nodes of node p and a and b are the linking coefficients of the global stiffness matrix and source term, respectively. The linking coefficient (a) at the node, where the temperature discontinuity occurs has been analyzed to investigate the cause of the discontinuity. The conductive and convective terms in (52) determine the linking coefficients.

From physical considerations, the component of the convective term normal to the wall should be zero. However, the FEM approach violates this constraint wherever there is a circumferential variation in film thickness, as caused by tilting of a pad and/or eccentricity of the journal. This causes a fictitious convective wall heat flow (heat loss) as depicted in Fig. 19(*b*). This is because the Reynolds model assumes a zero y-direction (film thickness direction) velocity, and the convective wall heat flow is evaluated only

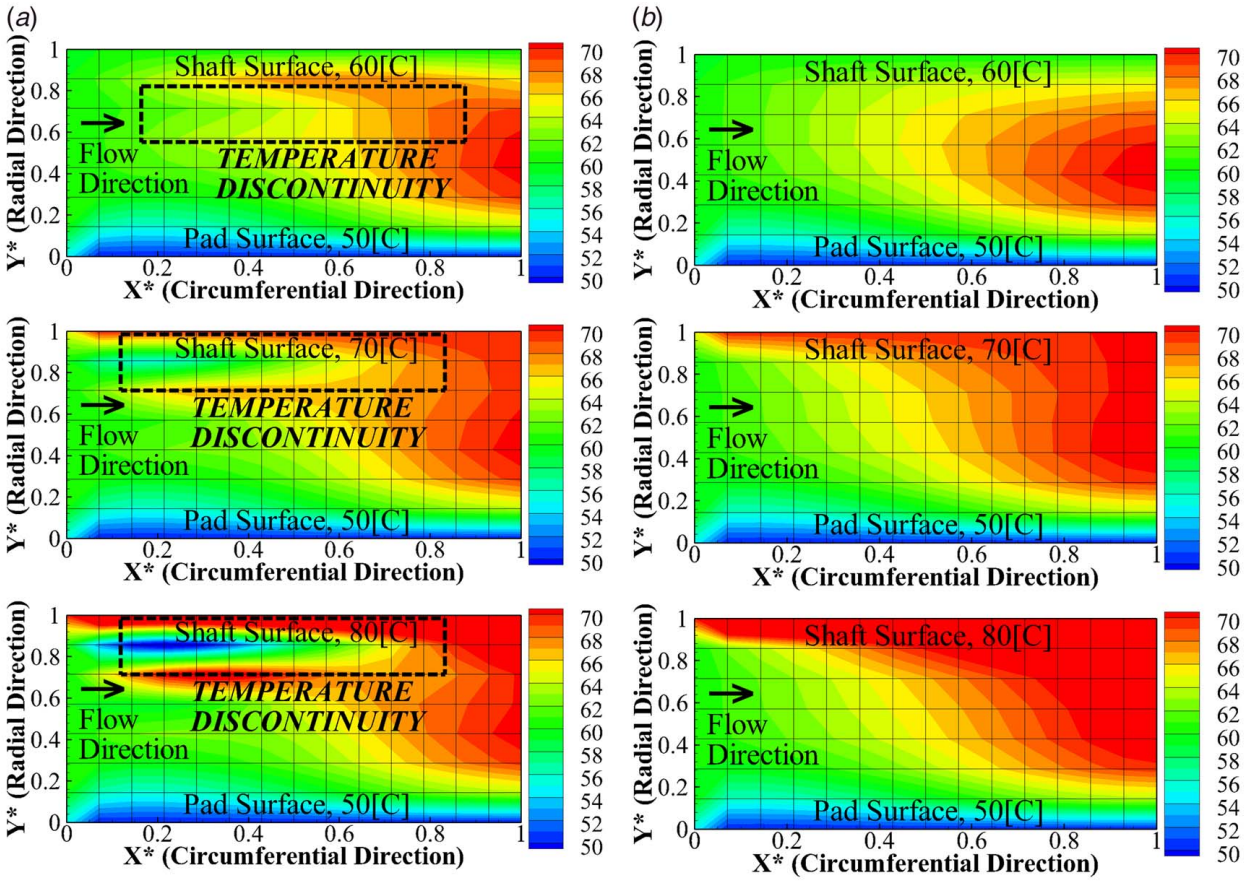

Fig. 18 Fluid-film temperature fields at pad 1 mid-span versus shaft surface temperature with (*a*) FEM and (*b*) FVM

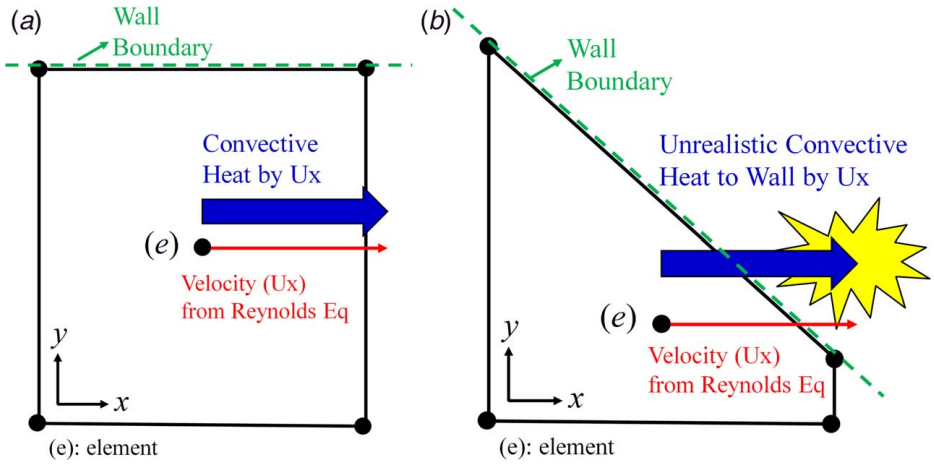

Fig. 19 Convective heat evaluated by Reynolds velocity solution: (*a*) non-wedge shape and (*b*) wedge shape

in the x-direction (circumferential) velocity. As illustrated in Fig. 18, the problem becomes severe if the flow inlet and wall temperatures have a large difference, since the wall convective heat loss is proportional to the prescribed wall temperature. Thus, the above constraint on flow direction causes the temperature discontinuity problem near the shaft wall. On the contrary, a uniform film in the circumferential direction does not show a film temperature discontinuity problem since the flow is always parallel to the wall, hence no convective wall heat flow, as shown in Fig. 19(*a*). The problem is exacerbated with high tilt pad angles, journal eccentricity, and speed. In contrast, the FVM eliminates the possibility of convective flow normal to a wall in all cases because the FVM formulation imposes a zero normal flow velocity condition at the shaft and pad surfaces.

It was confirmed that the use of denser grids with the FEM method, based on recent 3D modeling studies [7,20–22,26,29,30], will not mitigate the temperature discontinuity problem. The transformation of the lubricant gap to a parallel gap might improve the temperature discontinuity problem, and this will be investigated in the future work.

5 Results

5.1 Neural Network Axial Mixing Coefficient. The NN of axial MC is the regression model for obtaining the axial MCs and is used to calculate MLAMC in Sec. 2.2.3. The inputs for the NN consists of nine key parameters [23], including the film thickness and pressure at the IBP inlet and outlet, total pressure at the supply oil inlet, temperature at the IBP inlet, operating speed, journal radius, and bearing length. The outputs are the axial MCs at ten nodes uniformly distributed in the axial direction, along the half length of the axially symmetric bearing.

The axial MC outputs of the NN are denoted as the NNAMC. Axial MCs computed from CFD simulations are used to train the NN. As in the DOE presented in the previous work [23], CFD simulations were performed for 1536 parameter sets in the training set and 658 parameter sets in the test set. The training data set estimates the weighting and bias factors of the NN, and the test data set is utilized for the validation of the trained NN.

A convergence study was conducted on the number of hidden layer neurons, which is an essential parameter to achieve desired NN performance [23]. Figure 20 shows the performance results for a total of 21,940 axial MC samples at the ten axial nodes. There is a considerable improvement in accuracy between 5 and 25 neurons, as shown in Figs. 20(*a*) and 20(*b*). The best result occurs for 50 neurons as shown in Fig. 20(*c*). The mean squared error (MSE) and R^2 of the NNAMC confirm its accuracy. The MSE of the training data set is 3.6e-4. The MSE of the test data is 5.6e-4, and the R^2 is 1.0.

5.2 Static Variable and Dynamic Coefficient Results—Validation. The Reynolds/energy equation solution with the NNAMC approach is validated by comparing static variables and dynamic coefficients with an experimentally validated full CFD approach [15]. The conventional approach utilizing a FEM solution with user selected constant MC values is also included to illustrate its strong dependence on choice of MC, and its significant differences compared with the CFD- and NNAMC-based approaches. The choice of MC in the conventional approach typically depends on "industry practice" or "personal experience," which underlies

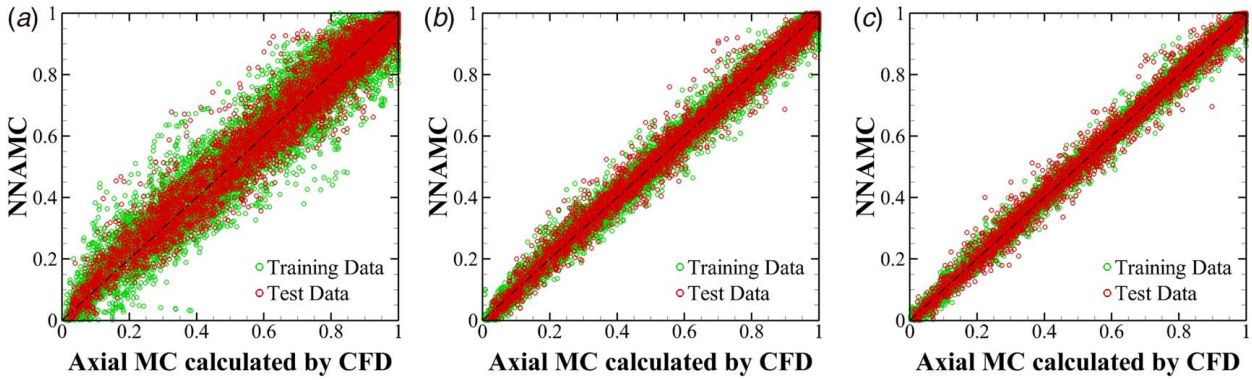

Fig. 20 Optimal NNAMC for increasing number of hidden layer neurons: (*a*) 5 neurons, (*b*) 25 neurons, and (c) 50 neurons

Table 6 Validation of CFD approach versus experiment [22]

	Mean error (%) between experimental and simulation		
Parameters	CFD	FEM-MC0.4	FEM-MC1.0
Eccentricity ratio	16.1	15.7	25.3
Peak loaded-pad T	4.2	7.6	4.3
Kxx	12.5	9.8	8.1
Kyy	6.7	10.5	9.2
Cxx	14.0	18.6	24.7
Cyy	11.2	20.7	26.5

the weakness of the approach. All results presented include the effects of pivot flexibility, pad flexibility, and thermal deformation of the solid domains.

Table 6 [22] confirms the efficacy of the CFD approach, as compared with experimental measurements [31,32]. The mean error is defined from the averaged relative error between the theoretical results and measurements. The CFD approach is seen to display much better agreement than the FEM approach, except for the x direction direct stiffness. "FEM-MC" indicates the FEM-based approach for the Reynolds and energy equations, utilizing a conventional (constant) MC model [7,20] to provide the fluid-film leading-edge temperature. The "CFD" approach utilizes a FVM-based solver to solve the Navier–Stokes and energy equations, without utilizing MC. The "FVM-HBP&MLAMC" is the FVM-based Reynolds approach presented in this study, which considers the 3D HBP coupled with the MLAMC. The FVM is a discretization method for solving the governing differential equations for fluid-film pressure and temperature. Yang and Palazzolo [23] introduced the MLMC to prescribe the fluid-film inlet temperature; however, the axial MC effect was not taken into account. In addition, Ref. [23] utilized an experience-based shaft surface temperature correction factor to account for neglecting radial temperature gradients at the pad leading edge. The temperature discontinuity issue discussed in Sec. 4 was noted in Ref. [23], but unlike the present work, did not address the radial temperature distribution at the fluid-film inlet. There is no need for a "shaft surface temperature correction factor" [23], and the film temperature discontinuity problem is eliminated, with the present approach.

Input parameter values are provided in Table 5, and the computational domains of the FVM-HBP&MLAMC model are depicted in Fig. 17. Nineteen and seven axial node rows are included with the half symmetry FVM-HBP&MLAMC and FEM models, respectively. The fewer number in the FEM case is justified due to the constant MC assumption.

Figure 21 show static (equilibrium) results, including the eccentricity ratio, averaged shaft temperature, and peak loaded-pad (Pad 5) temperature. The proposed FVM model shows remarkable agreement with all CFD results, validating its accuracy for static results. Figure 21(*a*) shows a lower eccentricity ratio for the CFD and FVM-HBP&MLAMC approaches compared with the conventional FEM approach. This results from the greater thermal expansion of the shaft in the former approaches, as indicated by the temperature results in Fig. 21(*b*). The higher journal expansion decreases the clearance, causing greater lift on the journal. The significantly higher averaged shaft temperature for the CFD and FVM-HBP&MLAMC approaches, relative to the FEM-MC 0.4 and 1.0 approach, results from the film temperature discontinuity problem and uniform temperature assumption at the fluid-film leading-edge. Figure 21(*c*) confirms the high accuracy of the FVM-HBP&MLAMC approach for predicting peak pad temperature.

Figure 22 shows the temperature fields over all computational domains and clearly confirms the higher shaft temperature in the FVM model. Figures 22(*a*) and 22(*b*) show uniform lubricant temperatures over the pad inlets in the conventional FEM models.

In contrast, Fig. 22(*c*) shows more realistic axial and radial lubricant temperature distributions [22] over the pad inlets. Figure 23 shows magnified views of temperature fields in the pad fluid-film domains. Figures 23(*a*) and 23(*b*) show that the pad inlet temperature conditions affect localized temperatures only near the pad inlets, resulting in strong temperature discontinuities in the FEM model. In contrast, the FVM-HBP&MLAMC approach results in Fig. 22(*c*) exhibit a continuous, global influence of pad inlet conditions throughout all pads. This approach accounts for the axial MC (oil inlet and side end effects) and radial temperature distribution effects at the pad inlets, and the resulting effects throughout all computational domains.

Figures 24 and 25 show the nondimensional dynamic coefficients and log decrement results in the x and y directions, respectively. Log dec values are obtained by considering a simple, lumped mass Jeffcott rotor model, with mass 1019 kg, and symmetrically supported by two identical bearings. The FVM model results show excellent agreement with the previously experimentally validated CFD work [22]. The increased radial heat flow into the journal, and resulting thermal expansion and clearance reduction, in the FVM-HBP&MLAMC model, yields larger stiffness and damping coefficients compared with the FEM-uniform MC model. The damping prediction accuracy in the FVM-HBP&MLAMC model is significantly better than the FEM-uniform MC approach.

The model validity has been confirmed for the tilt pad journal bearing with 101.8 mm diameter and 80 m/s surface velocity operating in laminar regime. Further investigation should be conducted for higher surface velocity bearings, operating in a fully turbulent regime.

The new approach presented provides a more accurate representation of the fluid film temperature at the pad leading-edge. This approach exhibits trends of larger rotordynamic coefficients, hotter shaft temperatures, and higher stability margins from the

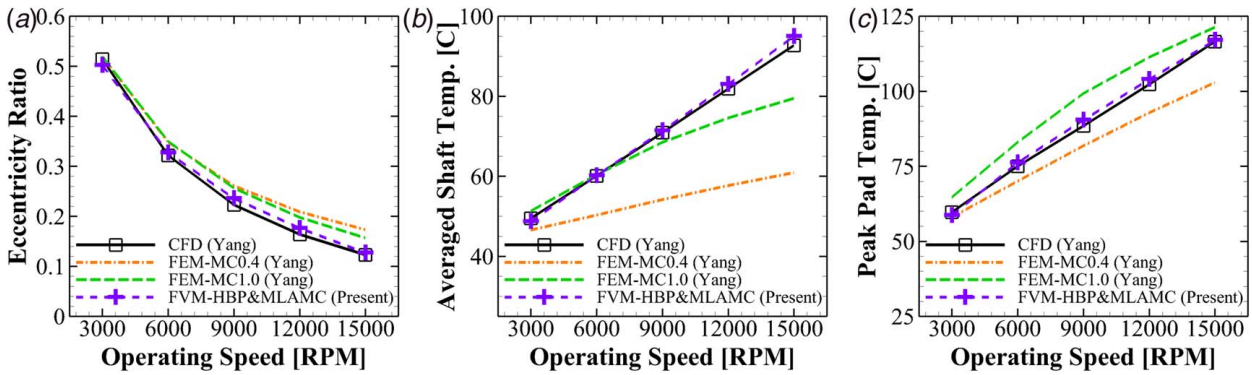

Fig. 21 Static results comparison with CFD [22] for (*a*) eccentricity ratio, (*b*) averaged shaft temperature, and (*c*) peak loaded-pad temperature

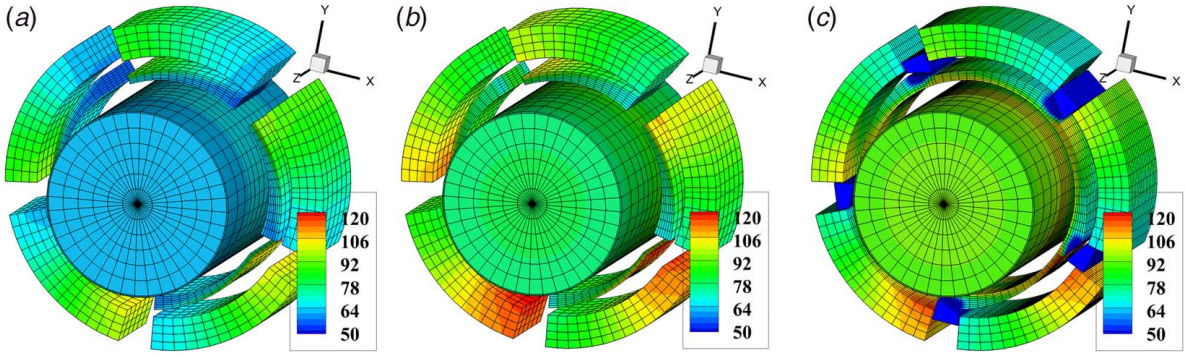

Fig. 22 Temperature contour comparison over the full computational domains between FEM and FVM: (*a*) FEM-MC0.4, (*b*) FEM-MC1.0, and (*c*) FVM-HBP&MLAMC

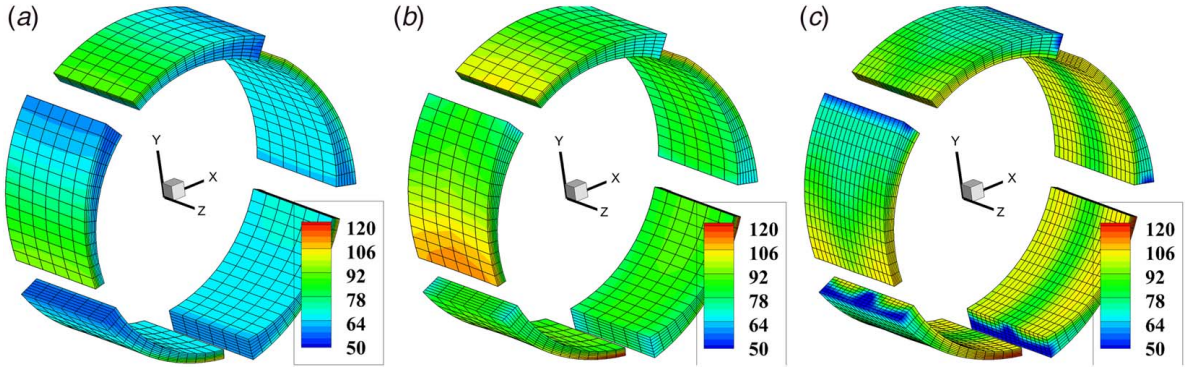

Fig. 23 Temperature contour comparison of fluid-film domains between FEM and FVM: (*a*) FEM-MC0.4, (*b*) FEM-MC1.0, and (*c*) FVM-HBP&MLAMC

log dec results, compared with the previous approaches. These trends should not be generalized to various oil injection types, and further investigation needs to be performed for the various injection types as future work.

6 Improvement of Computational Speed—Dynamic Coefficient Solver

The FVM-based Reynolds approach employs an efficient solver, specifically designed for the FVM discretized equations, instead of conventional LU decomposition, as discussed in Sec. 2.2.1. The time-consuming assembly process for the global matrices is eliminated in the FVM solver for the Reynolds and energy equations. The rotor and pad dynamic models require the most intensive computational load due to the time integration with a small time-step, while solving the discretized equations by the direct solver. Consequently, the efficient solvers for the Reynolds and energy equations significantly reduce computation time. An elapsed time comparison between the FEM and FVM models is performed to demonstrate this. The time taken for the state trajectories to reach their equilibrium value for a constant load is compared between the two approaches. Process 2 in Fig. 16(*a*) is executed once for this comparison, with the operating conditions: speed, 10,000 rpm; supply oil flow, 30 LPM. The novel solver exhibits significant improvement in the computation speed, as shown in Fig. 26.

The computation time acceleration becomes more pronounced as the grid density increases. Figures 21, 24, and 25 show close

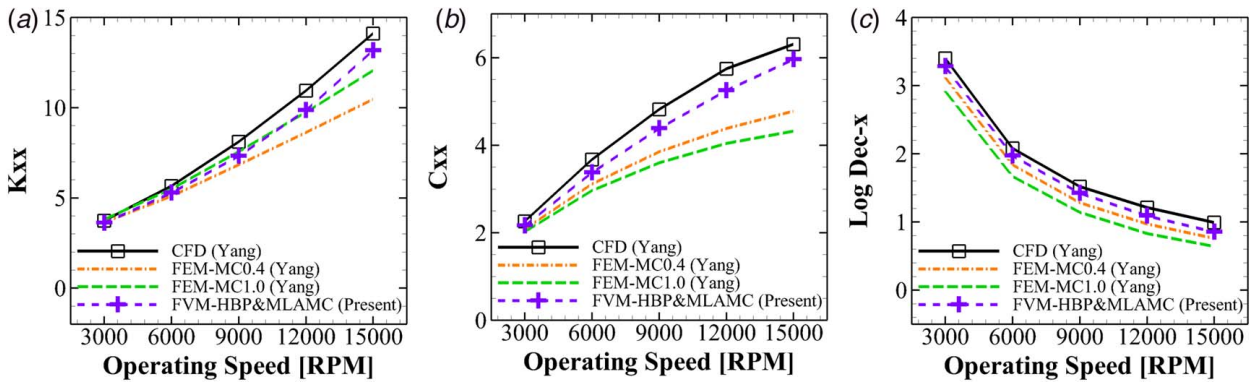

Fig. 24 Dynamic coefficient results (1) and comparison with CFD study [22]: (*a*) nondimensional stiffness, Kxx, (*b*) nondimensional damping, Cxx, and (c) log decrement-x

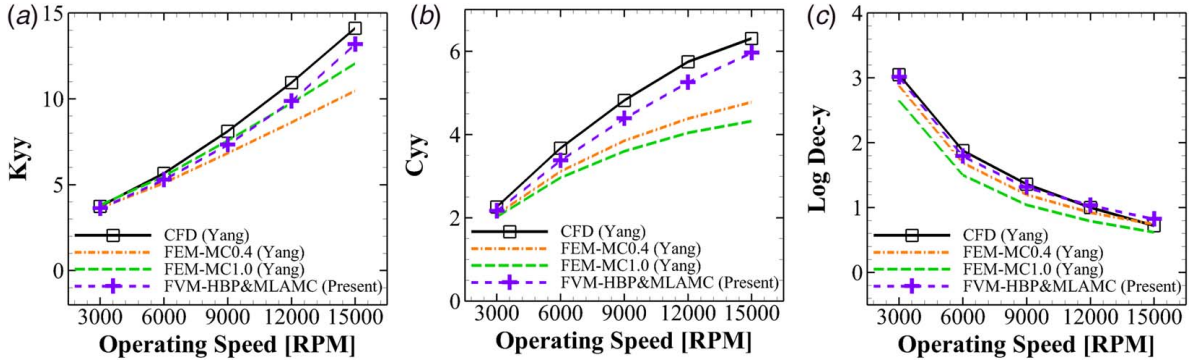

Fig. 25 Dynamic coefficient results (2) and comparison with CFD study [22]: (*a*) nondimensional stiffness, Kyy, (*b*) nondimensional damping, Cyy, and (*c*) log decrement-y

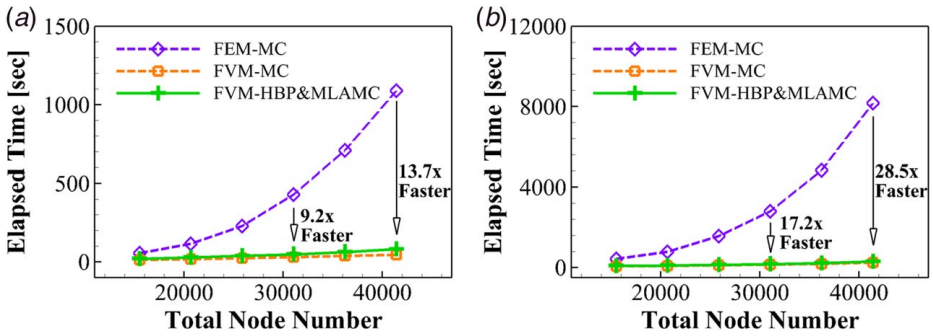

Fig. 26 Elapsed time for the dynamic coefficient solver to reach the steady-state equilibrium stage at 10,000 rpm, 30 LPM with (*a*) rigid pads and (*b*) flexible pad

Table 7 Total computational time of dynamic coefficient solver (Reynolds versus CFD)

Parameters	FVM-HBP&MLAMC (s)	CFD (s)	Comparison
Rigid pad	1049	186,221	178X faster
Flexible pad	3363	453,669	135X faster

agreement between the FVM-HBP&MLAMC approach and the full CFD modeling. Table 7 shows that FVM-HBP&MLAMC also executes far quicker than the full CFD model. Notably, the FVM-HBP&MLAMC is 178 times faster than the CFD solver with only minor loss in accuracy. The time in Table 7 is for the static solution plus dynamic coefficients. The proposed FVM-HBP&MLAMC approach provides considerable benefits in accuracy (versus FEM) and computation speed (versus FEM or CFD).

7 Conclusions

A novel approach for obtaining temperatures, steady-state equilibrium variables and dynamic coefficients of a TPJB's TEHD model was presented. The approach includes axial and radial lubricant temperature distributions at the pad leading-edge and their effects on static and dynamic response variables. Second, local violation of energy conservation and consequent temperature discontinuities were discovered in the FEM solution of the energy equation and resolved by using the FVM, which inherently satisfies local mass and energy conservation. The FEM deficiency persisted even with much finer meshes. The aforementioned shortcomings of the conventional FEM-uniform MC approach restrict heat flow from the film into the journal, resulting in lower journal temperatures and thermal expansions. This in turn was shown to have significant influence on increasing journal static eccentricity and decreasing stiffness and damping. As a consequence, it is recommended to utilize the conventional FEM-uniform MC approach only in cases where high fidelity results are not required, and journal thermal growth is anticipated to be negligible.

A novel HBP model was utilized for accurately and efficiently representing the mixing phenomena between pads. The HBP has a 3D modeled IBP subdomain and a 1D modeled OBP subdomain. The IBP model provides AMC and the radial and axial temperature distribution at the pad inlets. The AMC are also obtained from a novel DOE-CFD trained artificial neural network ML solution step. The benchmark for accuracy comparison in the examples was a full CFD model solution that was previously validated by comparison with experimental results [22]. The soundness of the CFD benchmark standard is also supported by the additional terms in its governing equations that are intentionally removed or simplified in the thin film Reynolds model. Results from the examples presented demonstrate a high level of agreement between the FVM-HBP&MLAMC approach and the full CFD derived results [22]. The conventional FEM-uniform MC approach on the other hand showed a high dependence on the MC value selected, and significant difference with the CFD model results.

A highly significant contribution was a computational algorithm that greatly accelerated computation time through the application of an efficient solving procedure in the discretized form of the Reynolds equation. The Reynolds equation is solved repeatedly in the coupled rotor-pad dynamics model, which magnifies the computational benefit from the new solving procedure. The FVM-HBP&MLAMC approach executes in approximately one tenth of the time required by the conventional FEM-MC approach. The new approach was also 178 times faster than the full CFD model approach and still yielded very similar results. In summary, the novel FVM-HBP&MLAMC approach demonstrated significant advances in TPJB-TEHD modeling accuracy and computational efficiency, including (1) considering the 2D (radial, axial) temperature distribution at the fluid-film, pad leading edge, (2) removing the MC value selection uncertainty or any assumed parameter on the BP region, and (3) accelerating computation speed while preserving similar accuracy to a full CFD model.

Acknowledgment

The authors appreciatively acknowledge the funding for this research from the Texas A&M Turbomachinery Research Consortium (TRC) and the Texas A&M High-Performance Research Computing Center (HPRC).

Conflict of Interest

There are no conflicts of interest.

Data Availability Statement

The authors attest that all data for this study are included in the paper. Data provided by a third party listed in Acknowledgment.

Nomenclature

P = pressure of fluid-film domain, Pa
h_f = film thickness, m
k_f = lubricant thermal conductivity, W/m K
u_{IB} = circumferential velocity of inner BP domain, m/s
v_{IB} = radial velocity of inner BP domain, m/s
w_{IB} = axial velocity of inner BP domain, m/s
w_{OB} = axial velocity of outer BP domain, m/s
x_{tp} = pad total x displacement by thermal deformation, m
x_p = pad total x displacement by dynamic model, m
x_{tr} = rotor total x displacement by thermal deformation, m
x_R = rotor total x displacement by dynamic model, m
y_{tp} = pad total y displacement by thermal deformation, m
y_p = pad total y displacement by dynamic model, m
y_{tr} = rotor total y displacement by thermal deformation, m
y_R = rotor total y displacement by dynamic model, m
z_{tp} = pad total z displacement by thermal deformation, m
z_p = pad total z displacement by dynamic model, m
z_{tr} = rotor total z displacement by thermal deformation, m
$C_{l,b}$ = radial bearing clearance, m
$C_{l,p}$ = pad bearing clearance, m
$C_{p,f}$ = lubricant specific heat, J/kg K
Q_{pnt} = pseudo penetrating flow, m^3/s
R_s = shaft radius, m
T_f = temperature of fluid-film domain, °C
T_{IB} = temperature of inner BP domain, °C
T_{OB} = temperature of outer BP domain, °C
T_P = temperature of pad domain, °C
T_R = temperature of rotor domain, °C
U_s = rotating shaft surface velocity, m/s
$\Delta\eta_I$ = axial mixing coefficient variation due to oil inlet effect
$\Delta\eta_E$ = axial mixing coefficient variation due to side end effect
η = axial mixing coefficient
η_{ml} = machine learning axial mixing coefficient
$\eta_{nn,c}$ = corrected neural network axial mixing coefficient
$\eta_{nn,0}$ = original neural network axial mixing coefficient
η_0 = original axial mixing coefficient in HBP model
$\eta_{nn,M}$ = corrected neural network axial mixing coefficient
μ_f = dynamic viscosity of lubricant, Pa s
ρ_f = density of lubricant, kg/m^3
ω_R = rotor spin frequency, rad/s

Appendix

Discretized Equation for Generalized Reynolds Equation (2D Quadrilateral Element). Discretized equation of generalized Reynolds equation for a 2D control volume:

$$a_P^P P_P = a_W^P P_W + a_E^P P_E + a_B^P P_B + a_T^P P_T + b^P$$

where

$$a_P^P = a_W^P + a_E^P + a_B^P + a_T^P,\ \ a_W^P = (D_{1,w}/\delta x_w)\Delta z,$$

$$a_E^P = (D_{1,e}/\delta x_e)\Delta z,\ \ a_B^P = (D_{1,b}/\delta z_b)\Delta x$$

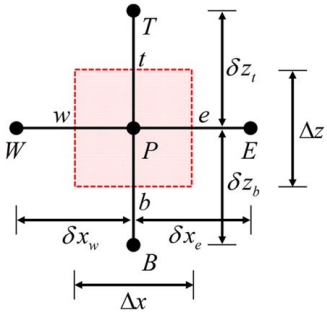

Fig. 27 2D control volume for generalized Reynolds equation: face index: *w*, *e*, *b*, *t*; volume index: *W*, *E*, *B*, *T*

$$a_T^P = (D_{1,t}/\delta z_t)\Delta x,\ \ b^P = (D_{2,e} - D_{2,w})U_s\Delta z + (\partial h/\partial t)_P\Delta x\Delta z$$

where D_1 and D_2 and film thickness (h) are given in Sec. 2.2.1 and U_s is the shaft surface velocity (Fig. 27).

Discretized Equation for Three-Dimensional Energy Equation in Fluid (3D Hexahedron Element)

Discretized equation of energy equation for a 3D control volume:

$$a_o\dot{T}_P + a_P^T T_P = a_W^T T_W + a_E^T T_E + a_S^T T_S + a_N^T T_N + a_B^T T_B + a_T^T T_T + b^T$$

where

$$a_W^T = D_w A_p(|P_w|) + \max[F_w, 0],\ \ a_E^T = D_e A_p(|P_e|) + \max[-F_e, 0]$$

$$a_S^T = D_s A_p(|P_s|) + \max[F_s, 0],\ \ a_N^T = D_n A_p(|P_n|) + \max[-F_n, 0]$$

$$a_B^T = D_b A_p(|P_b|) + \max[F_b, 0],\ \ a_T^T = D_t A_p(|P_t|) + \max[-F_t, 0]$$

$$a_P^T = a_W^T + a_E^T + a_S^T + a_N^T + a_B^T + a_T^T,\ \ a_o = \rho_f C_{p,f} V$$

$$b^T = \mu_f V((\partial u/\partial y)_P^2 + (\partial w/\partial y)_P^2)$$

where μ_f is the fluid dynamic viscosity and V is the volume of the element. F_w, F_e, F_s, F_n, F_b, and F_t are the convective heat flowrate

$$F_w = \rho_f C_{p,f} u A_w,\ \ F_e = \rho_f C_{p,f} u A_e,\ \ F_s = \rho_f C_{p,f} v A_s,\ \ F_s = \rho_f C_{p,f} v A_n$$

$$F_b = \rho_f C_{p,f} w A_b,\ \ F_t = \rho_f C_{p,f} v A_t$$

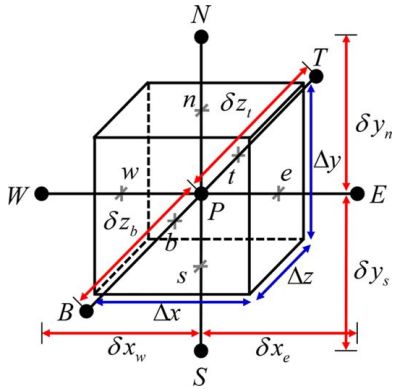

Fig. 28 3D control volume for 3D energy equation: face index: *w*, *e*, *s*, *n*, *b*, *t*; volume index: *W*, *E*, *S*, *N*, *B*, *T*

where A is the area at the face. The corresponding conductances are defined by

$$D_w = k_w A_w/\delta x_w,\ D_e = k_e A_e/\delta x_e,\ D_s = k_s A_s/\delta y_s,$$
$$D_n = k_n A_n/\delta y_n,\ D_b = k_b A_b/\delta z_b\ D_t = k_t A_t/\delta z_t$$

The Peclet number are $P_w = F_w/D_w$, $P_e = F_e/D_e$, $P_s = F_s/D_s$, $P_n = F_n/D_n$, $P_b = F_b/D_b$, and $P_t = F_t/D_t$. The function of A_p is determined by employing the power law scheme as $A_p(|P|) = \max\ [0, (1 - 0.1|P|^5)]$ (Fig. 28).

Three-Dimensional Finite Element Method Matrix for Structure Deformation (3D Hexahedron Element, Three Degrees-of-Freedom for 1 Node) [27,33]

$$\text{Mass matrix: } \underset{(24\times24)}{[M_{str,e}]} = \int_{-1}^{1}\int_{-1}^{1}\int_{-1}^{1} \rho_e \underset{(24\times3)}{[\psi_{str}]^T} \underset{(3\times24)}{[\psi_{str}]} \det\left(\underset{(3\times3)}{[J_{str}]}\right) d\xi_1 d\xi_2 d\xi_3$$

$$\text{Stiffness matrix: } \underset{(24\times24)}{[K_{str,e}]} = \int_{-1}^{1}\int_{-1}^{1}\int_{-1}^{1} \underset{(24\times6)}{[B_{str,e}]^T} \underset{(6\times6)}{[E_{str,e}]} \underset{(6\times24)}{[B_{str,e}]} \det\left(\underset{(3\times3)}{[J_{str}]}\right) d\xi_1 d\xi_2 d\xi_3$$

$$\text{Force vector: } \underset{(24\times1)}{\{F_{str,e}\}} = \int_{-1}^{1}\int_{-1}^{1}\int_{-1}^{1} \left(\underset{(24\times6)}{[B_{str,e}]^T} \underset{(6\times6)}{[E_{str,e}]} \underset{(6\times1)}{\{\varepsilon_{t0}\}} + \underset{(24\times3)}{[\psi_{str}]^T} \underset{(3\times1)}{\{\varepsilon_{c0}\}} \right) \det\left(\underset{(3\times3)}{[J_{str}]}\right) d\xi_1 d\xi_2 d\xi_3$$

where $\{\varepsilon_{t0}\} = \alpha(T - T_{ref})[1, 1, 1, 0, 0, 0]^T$ for thermal deformation and $\{\varepsilon_{c0}\} = [F_{c\xi_1}, F_{c\xi_2}, 0]^T$ for centrifugal force effect. ρ_e: solid density; physical coordinate axis: x_1, x_2, and x_3; natural coordinate axis: ξ_1, ξ_2, and ξ_3; ψ_{str}: shape function; $[J_{str}]$: Jacobian matrix with $J_{str,ij} = \partial x_i/\partial \xi_j$; $[E_{str,e}]$: constitutive relation matrix (isotropic material); F_c: centrifugal force; and $[B_{str,e}]$: coefficient matrix.

Three-Dimensional Finite Element Method Matrix for Structural Temperature (3D Hexahedron Element, One Degree-of-Freedom for 1 Node) [28]

Specific heat matrix:

$$C^e_{T,ij} = \int_{-1}^{1}\int_{-1}^{1}\int_{-1}^{1} \rho_e c_{p,e} \psi_i \psi_j \det\left(\underset{(3\times3)}{[J_T]}\right) d\xi_1 d\xi_2 d\xi_3$$

Heat conduction matrix:

$$K^e_{T,ij} = \int_{-1}^{1}\int_{-1}^{1}\int_{-1}^{1} k_e(\psi_{i,x_1}\psi_{j,x_1} + \psi_{i,x_2}\psi_{j,x_2} + \psi_{i,x_3}\psi_{j,x_3}) \times \det\left(\underset{(3\times3)}{[J_T]}\right) d\xi_1 d\xi_2 d\xi_3$$

where $\psi_{a,b} = \partial\psi_a/\partial b$. The shape function derivatives in physical coordinate should be transformed to natural coordinate derivatives before integration.

$c_{p,e}$: solid specific heat, k_e: solid thermal conductivity, ψ: Shape function, and $[J_T]$: Jacobian matrix with $J_{T,ij} = \partial x_i/\partial \xi_j$ for solid temperature.

References

[1] Lund, J., 1964, "Spring and Damping Coefficients for the Tilting-Pad Journal Bearing," ASLE Trans., **7**(4), pp. 342–352.

[2] Tieu, A., 1973, "Oil-Film Temperature Distribution in an Infinitely Wide Slider Bearing: An Application of the Finite-Element Method," J. Mech. Eng. Sci., **15**(4), pp. 311–320.

[3] Knight, J. D., and Barrett, L. E., 1987, "Analysis of Tilting-Pad Journal Bearing With Heat Transfer Effects," ASME J. Tribol., **110**(1), pp. 128–133.

[4] Brugier, D., and Pascal, M. T., 1989, "Influence of Elastic Deformations of Turbo-Generator Tilting Pad Bearings on the Static Behavior and on the Dynamic Coefficients in Different Designs," ASME J. Tribol., **111**(2), pp. 364–371.

[5] Taniguchi, S., Makino, T., Takeshita, K., and Ichimura, T., 1990, "A Thermohydrodynamic Analysis of Large Tilting-Pad Journal Bearing in Laminar and Turbulent Flow Regimes With Mixing," ASME J. Tribol., **112**(3), pp. 542–550.

[6] Kim, J., Palazzolo, A. B., and Gadangi, R. K., 1994, "TEHD Analysis for Tilting-Pad Journal Bearings Using Upwind Finite Element Method," Tribol. Trans., **37**(4), pp. 771–783.

[7] Suh, J., and Palazzolo, A. B., 2015, "Three-Dimensional Dynamic Model of TEHD Tilting-Pad Journal Bearing—Part I: Theoretical Modeling," ASME J. Tribol., **137**(4), p. 041704.

[8] Monmousseau, P., and Fillon, M., 2000, "Transient Thermoelastohydrodynamic Analysis for Safe Operating Conditions of a Tilting-Pad Journal Bearing During Start-Up," Tribol. Int., **33**(2), pp. 225–231.

[9] Fillon, M., Bligoud, J. C., and Frene, J., 1992, "Experimental Study of Tilting-Pad Journal Bearings—Comparison With Theoretical Thermoelastohydrodynamic Results," ASME J. Tribol., **114**(3), pp. 579–587.

[10] Fillon, M., and Bouyer, J., 2004, "Thermohydrodynamic Analysis of a Worn Plain Journal Bearing," Tribol. Int., **37**(2), pp. 129–136.

[11] Haugaard, A. M., and Santos, I. F., 2010, "Multi-Orifice Active Tilting-Pad Journal Bearings—Harnessing of Synergetic Coupling Effects," Tribol. Int., **43**(8), pp. 1374–1391.

[12] Brito, F. P., Miranda, A. S., Claro, J. C. P., and Fillon, M., 2012, "Experimental Comparison of the Performance of a Journal Bearing With a Single and a Twin Axial Groove Configuration," Tribol. Int., **54**, pp. 1–8.

[13] Lin, Q., Wei, Z., Wang, N., and Chen, W., 2013, "Analysis on the Lubrication Performances of Journal Bearing System Using Computational Fluid Dynamics and Fluid-Structure Interaction Considering Thermal Influence and Cavitation," Tribol. Int., **64**, pp. 8–15.

[14] Brito, F. P., Miranda, A. S., Claro, J. C. P., Teixeira, J. C., Costa, L., and Fillon, M., 2014, "The Role of Lubricant Feeding Conditions on the Performance Improvement and Friction Reduction of Journal Bearings," Tribol. Int., **72**, pp. 65–82.

[15] Ettles, C., 1969, "Hot Oil Carry-Over in Thrust Bearings," Proc. Instin. Mech. Eng., Conf. Proc., **184**(12), pp. 75–81.

[16] Mitsui, J., Hori, H., and Tanaka, M., 1983, "Thermohydrodynamic Analysis of Cooling Effect of Supply Oil in Circular Journal Bearing," ASME J. Lubr. Tech., **105**(3), pp. 414–420.

[17] Pinkus, O., 1990, *Thermal Aspects of Fluid Film Tribology*, ASME Press, New York, 187–197.

[18] Hagemann, T., and Schwarze, H., 2018, "A Model for Oil Flow and Fluid Temperature Inlet Mixing in Hydrodynamic Journal Bearings," ASME J. Tribol., **141**(2), p. 021701.

[19] Abdollahi, B., and San Andres, L., 2019, "Improved Estimation of Bearing Pads' Inlet Temperature: A Model for Lubricant Mixing at Oil Feed Ports and Validation Against Test Data," ASME J. Tribol., **141**(3), p. 031703.
[20] Yang, J., and Palazzolo, A., 2019, "3D Thermo-Elasto-Hydrodynamic CFD Model of a Tilting Pad Journal Bearing—Part I: Static Response," ASME J. Tribol., **141**(6), p. 061702.
[21] Yang, J., and Palazzolo, A., 2019, "3D Thermo-Elasto-Hydrodynamic CFD Model of a Tilting Pad Journal Bearing—Part II: Dynamic Response," ASME J. Tribol., **141**(6), p. 061703.
[22] Yang, J., and Palazzolo, A., 2020, "CFD Based Mixing Prediction for Tilt Pad Journal Bearing TEHD Modeling——Part I: I TEHD-CFD Model Validation and Improvements," ASME J. Tribol., **143**(1), p. 011801.
[23] Yang, J., and Palazzolo, A., 2020, "CFD Based Mixing Prediction for Tilt Pad Journal Bearing TEHD Modeling——Part II: Implementation With Machine Learning," ASME J. Tribol., **143**(1), p. 011802.
[24] Armentrout, R. W., He, M., Haykin, T., and Arthur, R. E., 2017, "Analysis of Turbulence and Convective Inertia in a Water-Lubricated Tilting-Lubricated Tilting-Pad Journal Bearing Using Conventional and CFD Approaches," Tribol. Trans., **60**(6), pp. 1129–1147.
[25] Hagemann, T., Zeh, C., and Schwarze, H., 2019, "Heat Convection Coefficients of a Tilting-Pad Journal Bearing With Directed Lubrication," Tribol. Int., **136**, pp. 114–126.
[26] Suh, J., and Palazzolo, A., 2014, "Three-Dimensional Thermohydrodynamic Morton Effect Simulation—Part I: Theoretical Model," ASME J. Tribol., **136**(3), p. 031706.
[27] Palazzolo, A., 2016, *Vibration Theory and Applications With Finite Elements and Active Vibration Control*, Wiley, Chichester, UK.
[28] Cook, R. D., Malkus, D. S., Plesha, M. E., and Witt, R. J., 2002, *Concepts and Applications of Finite Element Analysis*, John Wiley & Sons. Inc., NJ.
[29] Tong, X., Palazzolo, A., and Suh, J., 2016, "Rotordynamic Morton Effect Simulation With Transient, Thermal Shaft Bow," ASME J. Tribol., **138**(3), p. 031705.
[30] Suh, J., and Palazzolo, A., 2015, "Three-Dimensional Dynamic Model of TEHD Tilting-Pad Journal Bearing—Part II: Parametric Studies," ASME J. Tribol., **137**(4), p. 041704.
[31] Carter, C. R., 2007, "Measurement and Predicted Rotordynamic Coefficients and Static Performance of a Rocker-Pivot Tilt Pad Bearing in Load-On-Pad and Load-Between-Pad Configurations," M.S. thesis, Mechanical Engineering, Texas A&M University, College Station, TX.
[32] Kulhanek, C. D., 2010, "Dynamic and Static Characteristics of a Rocker-Pivot, Tilting-Pad Bearing With 50% and 60% Offsets," M.S. thesis, Mechanical Engineering, Texas A&M University, College Station, TX.
[33] Oh, J., Palazzolo, A., and Hu, L., 2020, "Stability of Non-Axisymmetric Rotor and Bearing Systems Modeled With Three-Dimensional-Solid Finite Elements," ASME J. Vib. Acoust., **142**(1), p. 011010.